EFFECT OF BLEED OPENING RATIO ON FLOW STRUCTURE OF A NONSLENDER DELTA WING

A THESIS SUBMITTED TO
THE GRADUATE SCHOOL OF NATURAL AND APPLIED SCIENCES
OF
MIDDLE EAST TECHNICAL UNIVERSITY

BY

KAYACAN KESTEL

IN PARTIAL FULFILLMENT OF THE REQUIREMENTS
FOR
THE DEGREE OF MASTER OF SCIENCE
IN
MECHANICAL ENGINEERING

AUGUST 2019

Approval of the thesis:

EFFECT OF BLEED OPENING RATIO ON FLOW STRUCTURE OF A NONSLENDER DELTA WING

submitted by **KAYACAN KESTEL** in partial fulfillment of the requirements for the degree of **Master of Science in Mechanical Engineering Department, Middle East Technical University** by,

Prof. Dr. Halil Kalıpçılar
Dean, Graduate School of **Natural and Applied Sciences** ______________

Prof. Dr. M. A. Sahir Arıkan
Head of Department, **Mechanical Engineering** ______________

Assoc. Prof. Dr. M. Metin Yavuz
Supervisor, **Mechanical Engineering, METU** ______________

Examining Committee Members:

Assoc. Prof. Dr. Cüneyt Sert
Mechanical Engineering Dept., METU ______________

Assoc. Prof. Dr. M. Metin Yavuz
Mechanical Engineering Dept., METU ______________

Assist. Prof. Dr. Ö. Uğraş Baran
Mechanical Engineering Dept., METU ______________

Assist. Prof. Dr. Özgür Ekici
Mechanical Engineering Dept., Hacettepe University ______________

Assist. Prof. Dr. Onur Baş
Mechanical Engineering Dept., TED University ______________

Date:

I hereby declare that all information in this document has been obtained and presented in accordance with academic rules and ethical conduct. I also declare that, as required by these rules and conduct, I have fully cited and referenced all material and results that are not original to this work.

Name, Surname: Kayacan Kestel

Signature :

ABSTRACT

EFFECT OF BLEED OPENING RATIO ON FLOW STRUCTURE OF A NONSLENDER DELTA WING

Kestel, Kayacan
M.S., Department of Mechanical Engineering
Supervisor: Assoc. Prof. Dr. M. Metin Yavuz

August 2019, 97 pages

Boundaries of the aircraft industry need to expand since both economic and ecologic constraints are getting more challenging. The usage of Unmanned Air Vehicles (UAV), Unmanned Combat Air Vehicles (UCAV), and Micro Air Vehicles (MAV) which can be simplified as non-slender delta wing plan-forms has been increasing during the last few decades, primarily due to their superiority over commercial airplanes. Hence, researchers have aimed to control the complex flow structures on non-slender delta wings with particular interest on elimination of large-scale, three dimensional surface separation indication of pre-stall/stall regime, which appears at sufficiently high angle of attacks.

Recently, it is proposed that passive bleeding, which utilizes passage inside the wing in order to allow the fluid to flow from the pressure side to suction side by using inherent pressure difference, have potential to be used as a flow control method to eliminate large-scale surface separation. The aim of the present study is to understand the effect of bleed opening ratio on flow structure and aerodynamic forces of a non-slender, 45 degree swept delta wing. For that purpose, the delta wings with four different bleed opening ratios, *bor*, varying from 0.35 to 1.00, have been tested in a low-speed wind tunnel using surface pressure measurement, Particle Image Velocimetry (PIV), and force measurement. The experiments were conducted in a broad range of angles of attack $0 \geq \alpha \geq 36$ degree and at two different Reynolds number Re = 5 x 10^4 and 1 x 10^5.

The results indicate that at high angles of attack where the pronounced surface separation appears on the plan-form, wing with *bor=1.00* is the most successful in the elimination of the of large-scale, three-dimensional surface separation, albeit that the lift force over the wing decreases. Moreover, the wing with *bor=0.85* exhibits the best performance considering the lift coefficients and the stall angle. Further studies are needed to effectively use bleeding as a flow control technique.

Keywords: delta wing, bleeding, bleed opening ratio, flow control, non-slender, low sweep

ÖZ

AKITMA AÇIKLIK ORANININ İNCE OLMAYAN DELTA KANAT ÜZERİNDEKİ AKIŞA ETKİSİ

Kestel, Kayacan
Yüksek Lisans, Makina Mühendisliği Bölümü
Tez Yöneticisi: Doç. Dr. M. Metin Yavuz

Ağustos 2019 , 97 sayfa

Havacılık sektöründeki ekonomik ve ekolojik sınırlamaların artması ile birlikte, havacılık teknolojisi de sınırlarını geliştirmek zorunda kalmıştır. Basit delta kanat şeklinde modellenebilen insansız hava araçlarının ve mikro hava araçlarının kullanımı da, bu kanatların sıradan airfoil kullanan hava araçlarına göre olan üstünlüklerinden dolayı, son yıllarda artış göstermektedir. Bunun sonucu olarak, araştırmacılar, ince olmayan delta kanatlar etrafındaki karmaşık akış yapısının anlaşılması ve bu yapının kontrolü ile üç boyutlu yüzey ayrılmasını engellemek ve yüksek hücum açılarında görülen perdövitesi geciktirmek amacıyla çalışmalar yapmaktadırlar.

İnce olmayan delta kanatlar üzerinde yeni uygulanmaya başlanan pasif akıtma metodunun, üç boyutlu yüzey ayrılmasını engellemede etkili olabileceği görülmüştür. Pasif akıtma metodu, kanadın içindeki basit geçitler sayesinde, kanadın basınç ve emme yüzeyleri arasındaki basınç farkından faydalanara, havanın basınç yüzeyinden emme yüzeyine geçmesini sağlayan bir akış kontrol yöntemidir. Bu çalışmadaki amaç, pasif akıtma açıklık oranının, bor, ince olmayan, 45 derece ok açılı, delta kanatlar etrafındaki akış yapısına ve kanat üzerindeki aerodinamik kuvvetlere etksini incelemektir.

Bu amaçla, akıtma açıklık oranları 0.35 ve 1.00 arasında değişen dört farklı ince olmayan delta kanat, yüzey basınç ölçüm tekniği, parçacık görüntülemeli hız ölçüm tekniği ve kuvvet ölçüm teknikleri kullanılarak, düşük hızlı rüzgar tünelinde test edilmiştir. Deneyler, geniş bir hücum açısı aralığında $0 \geq \alpha \geq 36$ ve iki farklı Reynolds sayısında Re = 5 x 10^4 and 1 x 10^5 yürütülmüştür.

Çalışmanın sonucu göstermiştir ki, *bor=1.00* açıklık oranına sahip kanat, üç boyutlu yüzey ayrılmasını engellemekte en etkili performansı göstermiştir ancak kanat üzerindeki kaldırma kuvvetinde bir düşüş olduğu görülmüştür. Ayrıca, *bor=0.85* açıklık oranına sahip kanat, kaldırma kuvveti ve perdövitesin geciktirilmesi yönlerinde en başarılı performansı göstermiştir. Pasif akıtma yönteminin daha etkin bir akış kontrol mekanizması olarak kullanımı için, bu konuda ileri tetkikler yapılmalıdır.

Anahtar Kelimeler: delta kanat, düşük ok açısı, ince olmayan delta kanat, akıtma, akış kontrol

To my family

ACKNOWLEDGMENTS

I would like to express my sincerest appreciation to the people who support and motivate me during my work. To begin with, I am grateful to my thesis supervisor, Assoc. Prof. Dr. M. Metin Yavuz for his guidance and support. Apart from his academic guidance, he has always motivated me to go for the hard decisions in life and led me to participate in both national and international conferences, which eventually helped me widen my horizon and shaped my future.

This study and where I have come in my life would not have been possible without the support of my mother Emel Kestel and my sister Damla Kestel Erdoğan. Although they had no idea about what I had been working on specifically, they always encouraged me throughout my studies.

I would also like to thank my friends in our lab group Burcu Ramazanlı and Mohammad Sharifi Ghazijahani for sharing their experience about the study and their friendship.

Additionally, I should express my profound gratitude to Prof. Dr. Oğuz Uzol and Dr. Hooman Amiri for sharing really important equipment for this study and their technical guidance.

Finally, I am grateful for Mr. Mehmet Özçiftçi‘s technical assistance, which was one of the most important components of this study.

TABLE OF CONTENTS

LIST OF TABLES

TABLES

LIST OF FIGURES

FIGURES

LIST OF ABBREVIATIONS

Λ	Sweep angle
α	Angle of attack
θ	Back angle
ρ	Fluid density
A	Area of the suction side of the Base wing surface
S	Span length
s	Quarter span length
C	Chord length
u	Streamwise velocity component
v	Spanwise velocity component
ν	Kinematic viscosity
ω	Vorticity
V_{rms}	Velocity magnitude root-mean-square
C_L	Non-dimensional lift coefficient
C_D	Non-dimensional drag coefficient
C_p	Non-dimensional pressure coefficient
N	Number of samples in a measurements
p	Surface pressure measurement
$\overline{p}$	Average surface pressure
p_∞	Static pressure
bor	Bleed opening ratio
Ψ	Streamline
x	Chordwise distance from wing apex
y	Spanwise distance from wing symmetry line

z	Distance normal to the wing surface
U_∞	Free stream velocity
ω_i	Uncertainty estimate of a variable x_i
V	Vector field
Δt	Time difference between the two successive PIV images

CHAPTER 1

INTRODUCTION

Developments in the aircraft industry extended the limits of the aviation from the earliest design of the simple planes to the large scale fuel efficient commercial planes, supersonic fighters and micro air vehicles. Moreover, as the economic and environmental aims of the aerospace industry getting more challenging, need of various novel design of unconventional aircraft also stimulates engineering society to look for new the solutions [1]. Thin plan-form idea to minimize the drag arised at the early 1950s [2]. Accordingly, the desire to design a plane generating lift throughout the entire surface evolved the shape of the planes into the delta wing integrated air vehicles. Denning et al., at late 1990s, mentioned the possible benefits of integrating delta wing shape to large aircraft design , such examples of which are illustrated in Figure 1.1 [3]. Boeing blended-wing-body (BWB) airplane concept is an example of an unconventional aircraft design which is proved to be fuel efficient compared to conventional planes [4]. Furthermore, the usage of the Unmanned Air Vehicle (UAV), Unmanned Combat Air Vehicles (UCAV), and Micro Air Vehicles (MAV), which can be modeled as simple delta shaped plan-forms illustrated in Figure 1.2, augmented significantly in recent years. Since these micro devices are designed in the warrant to flee from the radars, the control surfaces over these aircraft are minimized. Furthermore, since they are highly susceptible to the loss of flight control under the exposure of gusts due to their low weight and small size, comprehension of the flow field of these plan-forms becomes crucial. Therefore, a thorough investigation of aerodynamics of non-slender delta wings and control of the flow structure over such plan-forms becomes the need [5, 6]. One of the first studies to comprehend flow structure around the simple plan-forms in delta shape with low-sweep angle was published in 1960s [7]. Despite that, over the years, many studies have been performed to comprehensively understand the complicated flow field of the non-slender delta wings and various methods of flow control were introduced to identify how they effect the flow field, which strongly influence the flight performance and stability, there are plenty of new control methods that are not applied to the non-slender delta wings.

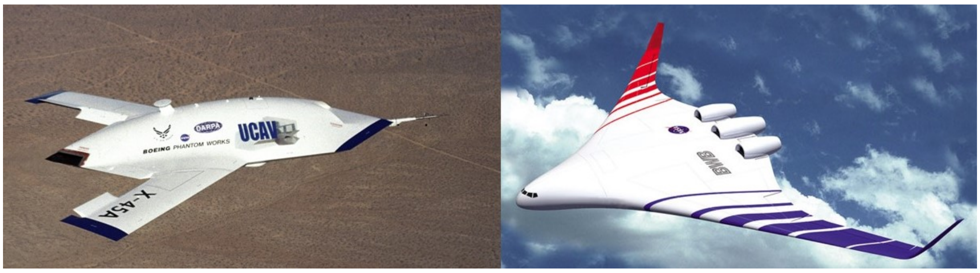

Figure 1.1: Illustration of Unmanned combat air vehicle UCAV[1](left) and the blended wing body BWB[2](right)

Figure 1.2: Representation of UAV, MAV, and UCAV [8]

The name of the delta wing is coming from the greek letter delta, Δ, due to the evident similarity of the shape of the plan-form. The sweep angle, Λ, shown in the schematic of a delta wing in Figure 1.3, is the main parameter classifying the delta wings. Although, even the slight changes of the sweep angle differ the aerodynamics and the flow field of these plan-forms, delta wings are basically classified into two according

[1]Retrieved from https://www.nasa.gov/centers/dryden/research/X45A/index.html
[2]Retrieved from https://www.nasa.gov/centers/langley/news/factsheets/FS-2003-11-81-LaRC.html

to their sweep angles: slender wings with sweep angle more than 55° and non-slender wings with that less than 55°. The superiority of non-slender delta wings over the slender ones appear in the low structural-weight-to-takeoff-weight ratio and high maneuverability capacity, nonetheless, number of studies regarding the flow physics of slender delta wings are far more than that of their non-slender counter-parts [8].

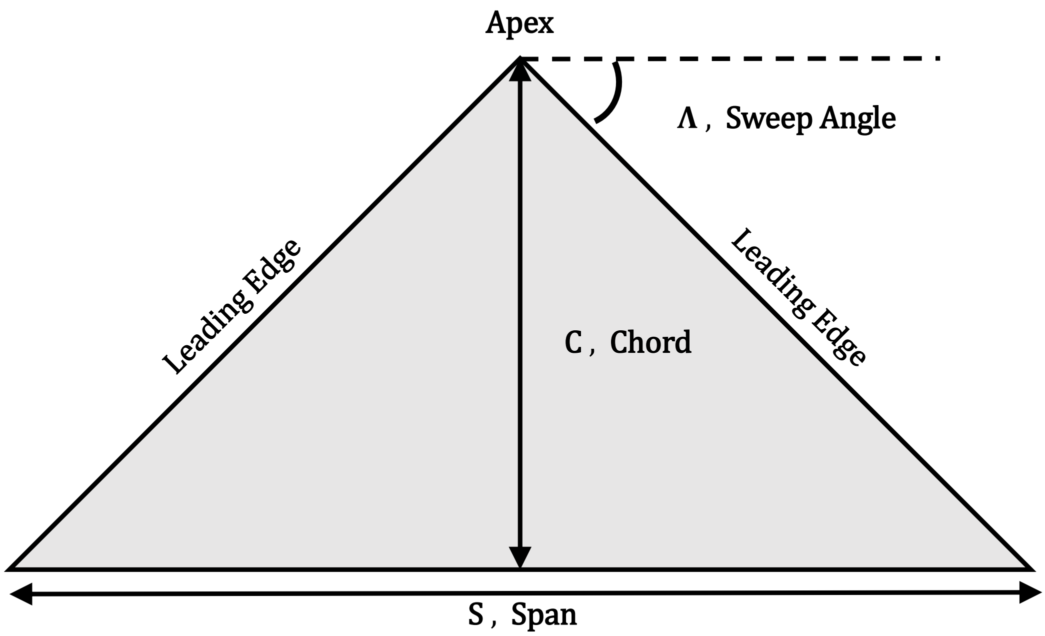

Figure 1.3: Basic schematic of a delta wing

Two counter rotating vortices are formed at the suction side of the delta wings regardless of the sweep angle of the wing [9]. As the velocity of the core of the vortices are higher than the free stream velocity, U_∞, presence of the vortices augments the lift force over the wing. For different flight conditions, as the flight speed and the attack angle, α, changes, the flow field dominated by the vortices faces instabilities, in addition, due to the adverse pressure gradient, the vortex might burst [10]. In Figure 1.4, the representation of the vortex formation, non-dimensional pressure coeffcient, $-C_p$, distribution along a spanwise direction, and the vortex burst mechanism are illustrated in detail.

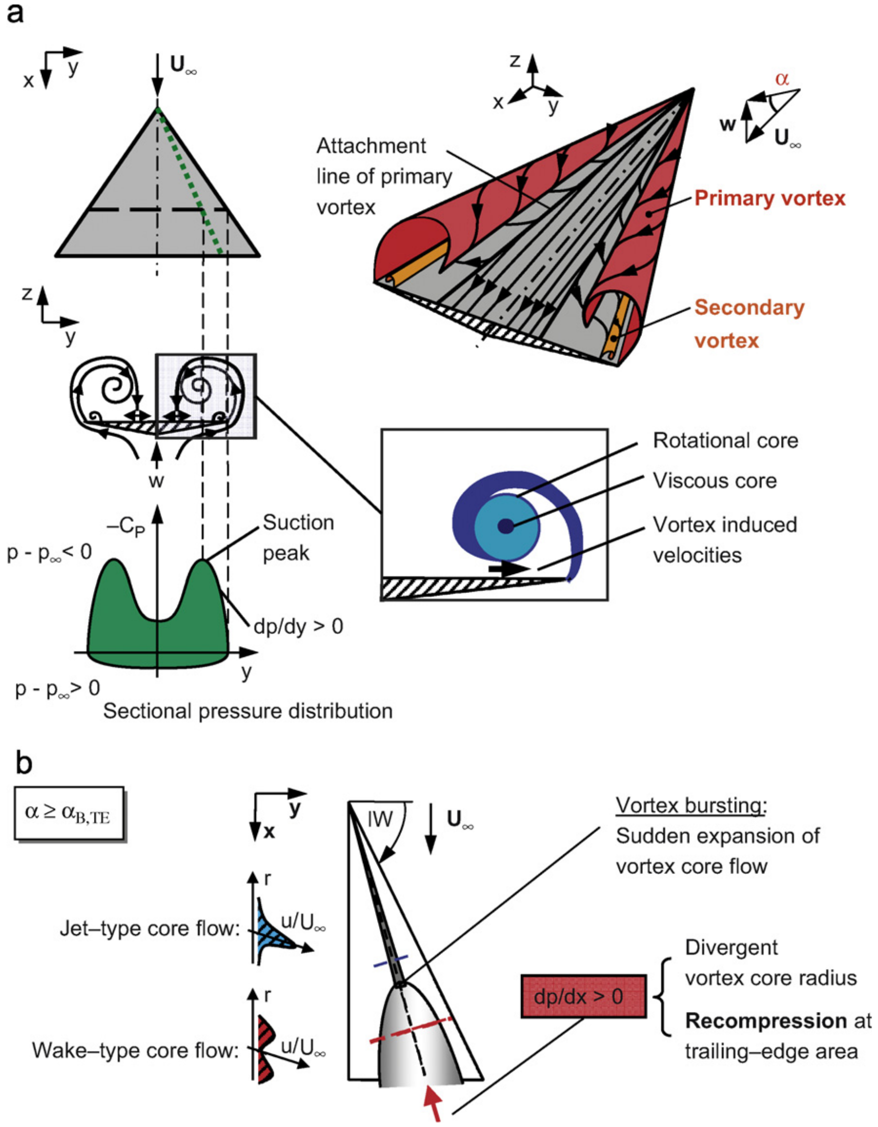

Figure 1.4: Vortex formation over a delta wing (a) and vortex burst (b) [11]

Stream encountering the leading edge of the plan-forms experiences separation, forming the vortical structure at the suction side. This separated shear layer further reattaches to the wing surface, for slender delta wings at very low attack angles and for non-slender ones at a wide range of attack angles [5,8].Reattachment, particularly for non-slender delta wings, is an important phenomenon as a proof of the stable coherent vortex structure, hence, a stable flight condition. Line of reattachment is observed at the outboard of the symmetry line and with the increasing angle of attack, line of reattachment advances to line of symmetry [8]. Further increase of the angle of attack eventually leads the reattachment to disappear. In Figure 1.5, detailed illustration of reattachment line and shear layer formation are presented. Viscous flow theory states that the presence of the adverse pressure gradient results in the separation of the flow. Flow separates from the wing surface at the pre-stall regime and the feature called "whorl" is observed [12]. At adequately high angles of attack, delta wing experiences the three dimensional separation. Figure 1.6 demonstrates the surface streamline structure for two distinct delta wings with different thickness-to-chord ratios. The one on the left-hand side of the figure exhibits the streamline structure of an attached flow, while on the right-hand side flow with "whorl" feature that experiences the three-dimensional separation is shown.

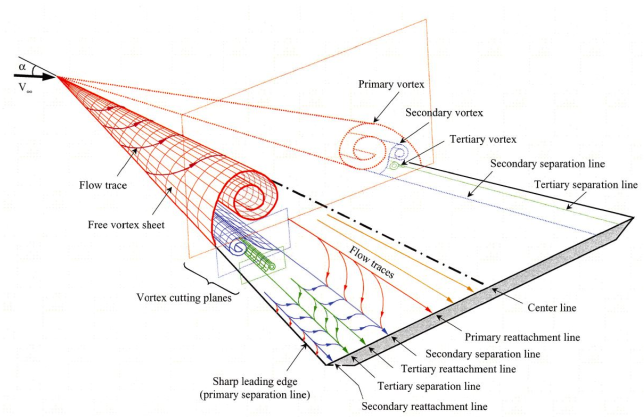

Figure 1.5: Explicit illustration of the reattachment line and the vortex formation [13]

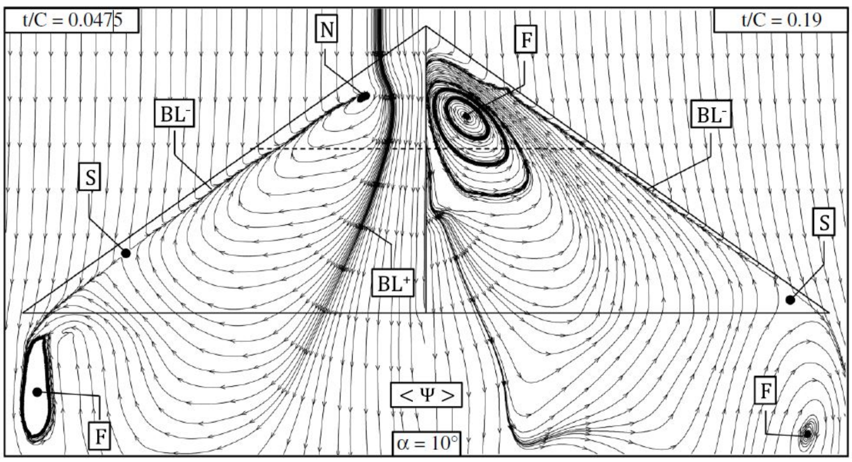

Figure 1.6: Streamlines over the plane in the vicinity of the suction surface of two different non-slender delta wing with different thickness at $\alpha = 10°$ [14]

At different flight conditions and under the exposure of strong gusts, for a stable and safe flight, the flow field around the delta wing must be well understood, moreover, it must be controlled such a way that the reattachment is satisfied, vortex burst is diminished or its location is retarded, and stall regime is delayed. Instabilities after the vortex burst locations and due to the lack of reattachment of the flow field, the planforms are exposed to high buffeting loads, fatigue damage and structural vibrations [10]. Hence, control of the flow field has utmost importance. Active and passive flow control techniques are introduced to shape the flow field in various engineering applications. Active control methods require energy input to the system while passive ones differentiate from the active methods in terms of the energy input requirement which is zero. In this present study, the control named passive bleeding is applied to a non-slender wing to explore the effect of bleed opening ratio to the flow field.

Bleeding is a flow control method that has been applied on slotted wings and ailerons. The mechanism of this flow control method is to make use of the pressure difference between the suction and the pressure sides of the delta wing in order to transfer momentum through the openings over the wing to overcome the separation. Although the momentum transfer occurs due to the inherent pressure difference between the wing sides, this method can be applied both actively and passively considering whether the bleed passages are changing orientation or not. A simple sketch for bleeding is shown in Figure 1.7.

Figure 1.7: Illustration of a simple bleed mechanism through an airfoil [15]

1.1 Motivation of the Study

In the very recent paper, Çelik et al. proved that the passive bleeding is capable of satisfying the reattachment of the flow field at the pre-stall/stall regime [16]. The effect of passive bleeding investigated by introducing the bleed passages over a 45° swept delta wing. Three different orientation of bleed angles named as Back (B), Edge (E), and Back-Edge (BE) are implemented over the wings and flow field of the bleed controlled wings are compared with that of the Base wing which is lack of bleed openings. Figure 1.8 is taken from the paper and shows the findings for the Base wing on the left and bleed controlled wing with Back angle configuration on the right. Considering the smoke flow visualizations on top, both surface and cross flow visualizations exhibit that the recovery of the vortical structure is achieved with Back angle bleeding whereas vortex burst is observed over the Base wing at a position near the apex. In addition, crossflow non-dimensional vorticity results obtained via PIV approve the visualization images such that the vorticity intensity is higher in controlled wing, moreover, the non-dimensional vorticity pattern of the shear layer is elongated. Furthermore, non-dimensional pressure coefficient, $-C_p$, graphs at the bottom of Figure 1.8 has the foot-prints of the recovery of the vortices that holds the hump-like shape where the peak in the graph shows the maximum suction point, in other words, core of the vortex where the velocity is the highest. Thus, Back angle passive bleeding orientation is the most effective among others studied in the research. In the thesis study of Karagöz, 45 degree swept four delta wings with three different Back angle configurations are investigated. The Back angles are selected as 13, 18 and 23 degrees and among three wings, the plan-form with 23 degree Back angle passive bleeding configuration appeared as the most efficient in enhancing the flow field [17]. In this study, passive bleeding with Back orientation is also implemented on the 45 degree swept delta wings. Yet, the openings of the bleed passages vary and the aim is to comprehend the effect of bleed opening ratio to the flow field at the extremities of the flight conditions where the angle of attack is sufficient enough to lead the Base wing to experience the three-dimensional separation. Moreover, these two aforementioned studies has a gap in the investigation of the aerodynamic forces. Since the basis of bleeding is transferring the flow from pressure side to suction side, mechanism is expected to inherently decrease pressure difference between the two sides of the wing, hence, lift force might decrease as well. Moreover, information regarding the consequence of bleed application on the drag force and lift-to-drag ratio is missing in these two previous studies. Although, in both studies, flow fields are enhanced and recovery of the vortical structure is achieved in the pre-stall regime, in the absence of the force measurement, interpretation of delay of stall is not possible. Therefore, one of the goal of the present study is also to enlighten this ambiguity.

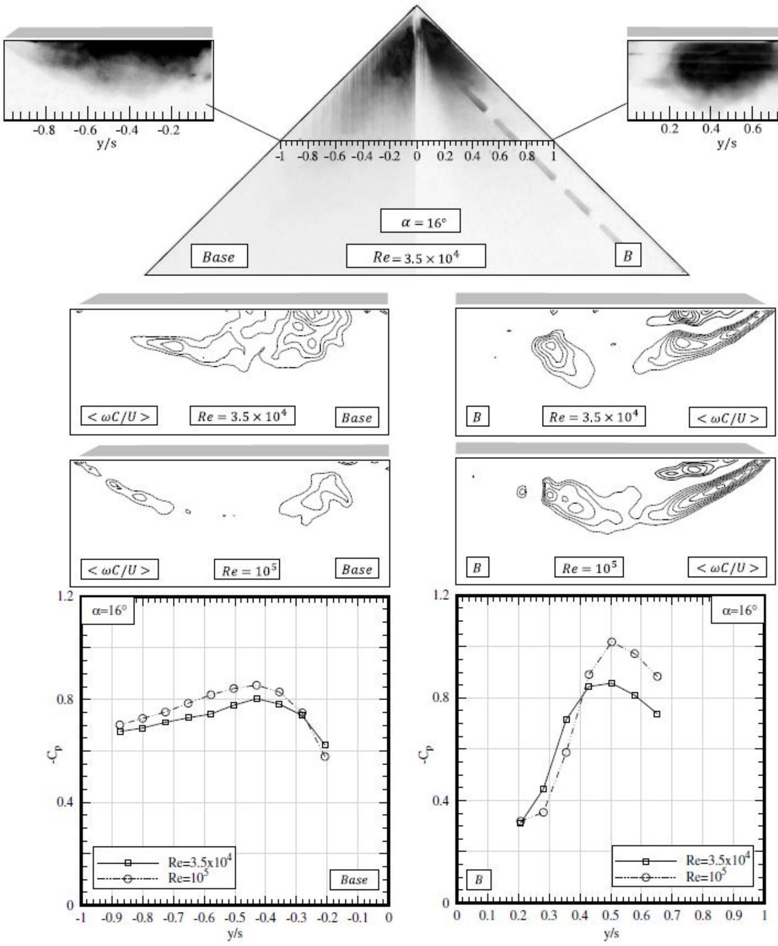

Figure 1.8: Smoke flow visualization, surface pressure measurement and PIV results of the 45° delta wing for base plan-form and passive bleed controlled plan-form [16]

1.2 Aim of the Study

As it is expressed above, passive bleeding is implemented on the 45° swept delta wings and the bleed passages over the plan-forms are selected to have the orientation of Back which is defined in the related article [16] and the Chapter 3 of this thesis. For this present research, four different wings with bleeding passages at different sizes were used to understand effect of the changes in the bleed opening ratio to the flow field of a 45° swept delta wing in the pre-stall/stall and three-dimensional separation regime. Moreover, the missing part in the related article, which is very significant in aircraft design, force measurements to obtain lift and drag coefficients are also studied in this thesis. Hence, flow field around the base wing is compared with the flow field around the bleed controlled wings to investigate the how the bleed opening ratio effects the aerodynamics of a non-slender delta wing at pre-stall/stall regime. Bleed-opening-ratio, *bor*, is defined as the ratio of the opening area of a wing to area of the maximum possible opening area. Maximum opening area is limited to 3 mm width and 121 mm length. Four wings with *bor* = 0.35, 0.60, 0.85 and 1.00 are used in the study. For this purpose, an experimental approach utilizing surface pressure measurement, particle image velocimetry (PIV), and force measurements is used.

1.3 The Outline of the Thesis

Formation of the thesis includes five main chapters.

In chapter one, introductory knowledge regarding the delta wings is given. Moreover, motivation and clear goal of the present study are also introduced to the reader.

The second chapter consists of the summary of the extensive literature survey about the vortex dominated flows, aerodynamics of both slender and non-slender delta wings, and flow control methods.

In chapter three, experimental set-up and wing design are discussed in detail. Moreover, the measurement techniques utilized during the study are also introduced comprehensively. The chapter ends with the experimental matrices and uncertainty estimates of the present measurement devices.

Chapter four exhibits and discusses the findings of the surface pressure measurements, near surface PIV, and force measurements.

The fifth chapter finalizes the research by explicitly explaining the conclusions obtained during the study, furthermore, presents the possible extensions for the future work.

CHAPTER 2

LITERATURE SURVEY

Following chapter extensively summarizes the studies in the literature regarding the flow structure around the delta wings and the flow control techniques.

2.1 Flow Structure around a Delta Wing

2.1.1 Vortical Structure

Flow structure of both slender and non-slender delta wings are dominated by the two counter rotating vortices that are separated from the leading edges of the wing [9], [7]. These vortices called primary vortices are formed as discrete vortex sheets as illustrated in Figure 2.1. Example of a vortex formation and coherent vortex layers, obtained with flow visualization, are also shown in Figure 2.2 and Figure 2.3, respectively. Despite that flow structure of both slender and non-slender delta wings are vortex dominated, there are notable differences.

As the sweep angle increases, the significant rise of lift also is observervered [7], moreover, the velocity at the core of the vortices increases with the escalating sweep angle and velocity at the core can be 4 - 5 times higher than the free stream velocity for slender delta wings [8]. In the analytical study of Polhamus [20], it is predicted that the lift produced with the contribution of the vortices can reach the 50% of the total lift over the wings with high sweep angles. Furthermore, the vortex structure of highly swept delta wings are stronger and less depedent the Reynolds number whereas that of low swept delta wings are sensitive to Reynolds number [21] . The major difference between high and low swept delta wings is that vortices are closer to the wing

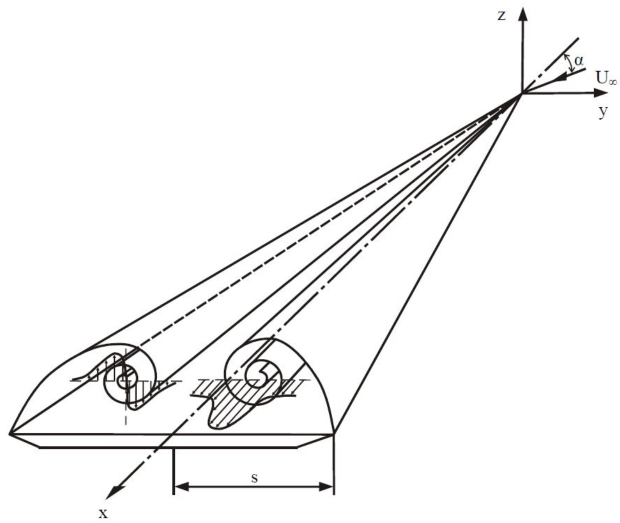

Figure 2.1: Illustration of the discrete vortex sheet [10]

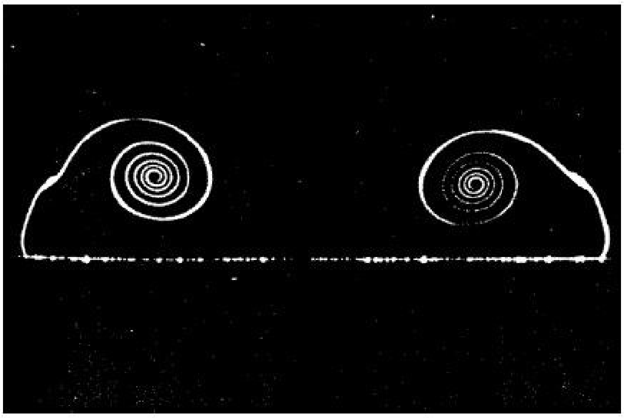

Figure 2.2: Generation of the vortices separated from the leading edge [18]

surface in a low swept delta wings compared to the high swept ones [22]. This distinction results in the interaction of wing surface and vortices and it generates the secondary vortex at the same sign vorticity with primary one at low Reynolds numbers and low angles of attack [23] . At high angles of attack, the secondary vortex tends to erupt and the flow structure becomes similar to the ones of highly swept delta wings. Illustration of dual vortex structure is demonstrated in Figure 2.4.

Figure 2.3: Crossflow visualization of coherent vortex sheet [19]

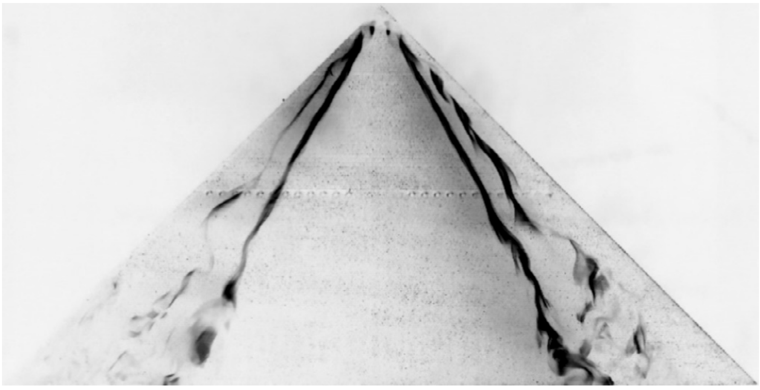

Figure 2.4: Illustration of dual vortex structure [24]

2.1.2 Vortex Breakdown

Phenomenon of vortex breakdown is defined as the sudden expansion of the vortical structure due to the rapid deceleration of the axial velocity at the vortex core [10], demonstrated in Figure 2.5, as a result of the adverse pressure gradient over the planforms [25]. This phenomenon is observed at high attack angles. Vortex breakdown is not unique to delta wings; hence, there exist seven different vortex breakdown types [26]. Among seven, three particular types as spiral, bubble, and double helix are observable over the delta wings. These three common types are shown in Figure 2.6. Pressure gradient and the swirl level appear to be the two main parameters that influence the presence and the location of vortex breakdown [10]. For slender delta wings, vortex breakdown location is visualized by Payne and it is shown that for a given attack angle location of vortex breakdown advances towards to trailing edge as sweep angle rises [27]. Moreover, Zharfa et al. demonstrated that, on a delta wing with a low sweep angle, increase in attack angle leads the location of breakdown to approach to the apex of the wing [28]. This phenomenon is undesired since the disruption of vortex results in significant drop in lift force, particularly for high swept delta wings. Although the lift contribution of vortex is not high at low swept delta wings, high buffeting loads occurring as the outcome of the vortex breakdown leads fatigue damage and structural vibrations [10].

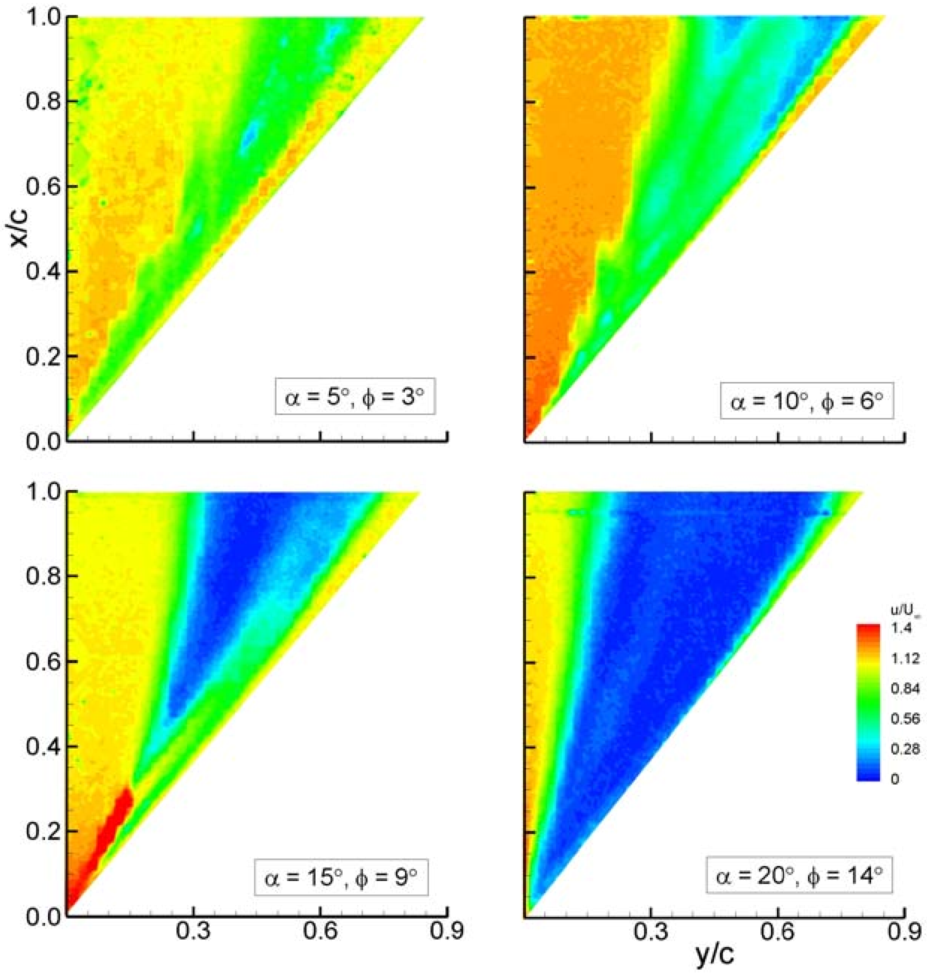

Figure 2.5: Velocity magnitude in a plane through vortex core [12]

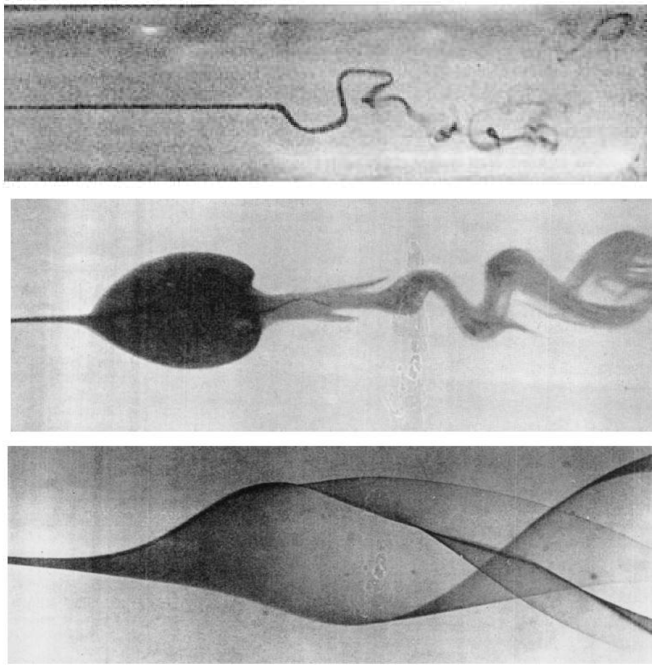

Figure 2.6: Visualization of spiral, bubble and double helix vortex breakdown types shown from top to bottom [26]

2.1.3 Shear Layer Reattachment

Differences in flow structure between slender and non-slender delta wings appear in the shear layer reattachment character as well. Highly swept delta wings experience the reattachment only at very small attack angles and after a certain attack angle the flow does not attach anymore [5]. Hence, the control of the reattachment over slender delta wings becomes difficult. On non-slender delta wings, location of reattachment of the leading-edge vortices to the wing surface, on the other hand, is outboard of the wing symmetry plane; moreover, reattachment line advances to the center line of the wing as the attack angle rises [8]. Honkan and Andreopoulos also proved that the region around the reattachment line has high turbulence intensity [29], accordingly, the location of the region with the high magnitude of rms velocity exhibits the approach of the reattachment line towards the center line of the wing in Figure 2.7. As incidence reaches a certain point near stall condition, reattachment is observed at the symmetry plane of the wing [30]. As mentioned, the highest velocity fluctuations in the vicinity of the wing surface are present along the reattachment line; thus, reattachment is said to be the most important source of buffeting, rather than the vortex burst in the pre-stall regime [12].

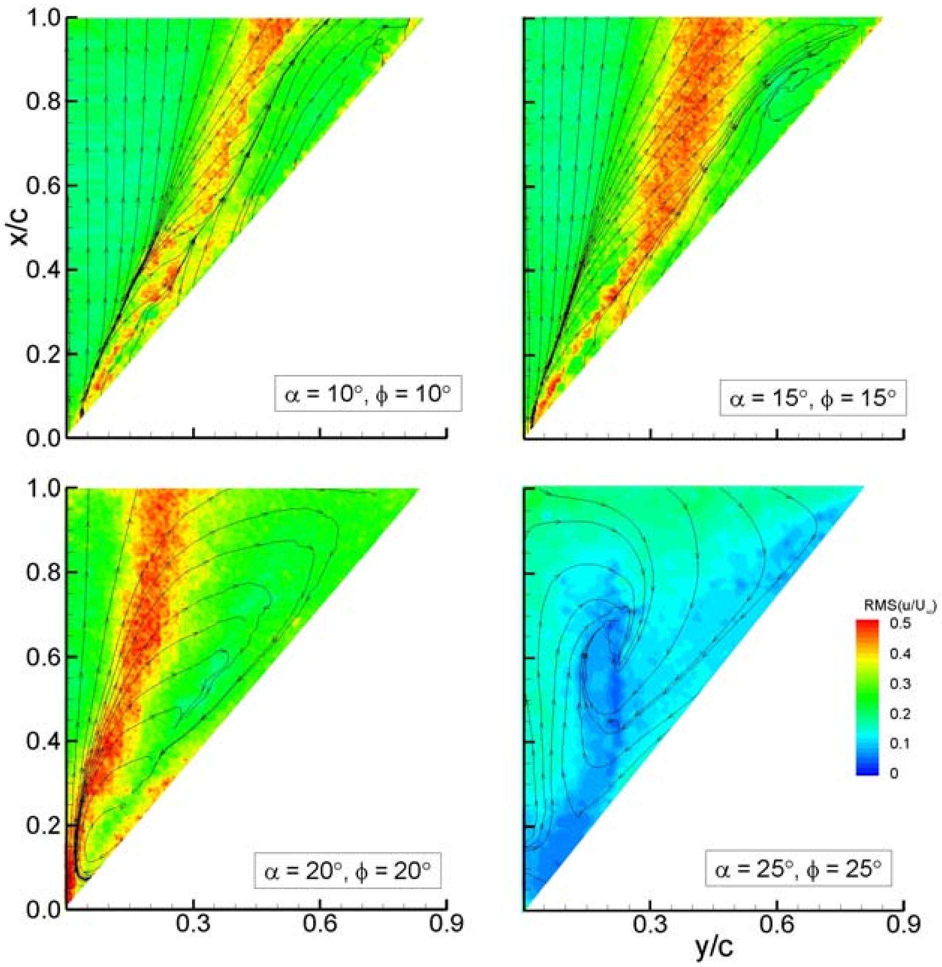

Figure 2.7: Magnitude of rms velocity near the wing surface [12]

2.1.4 Three Dimensional Flow Separation/Stall

According to the viscous flow theory, presence of adverse pressure gradient leads flow to separate. This phenomenon is also observed over the delta wings just before the stall condition. In Figure 2.8, streamlines structures over delta wings with flow reattachment and separated flow with "whorl" flow feature are demonstrated at different attack angles [12]. At sufficiently high incidences, vortical structure around the delta wing becomes prone to lose its characteristics and is replaced by a large-scale, surface streamline structure of inward-swirling, flow pattern, which is basically the major indicator of the three-dimensional separation [31]. Further increase in the incidence results in the stall where the "whorl" is observed. In the case of stall, reattachment of the shear layer is no longer possible, lift over the wing drops, and velocity in the vicinity of the plan-form converges to an almost stagnant one as it is demonstrated in Figure 2.8.

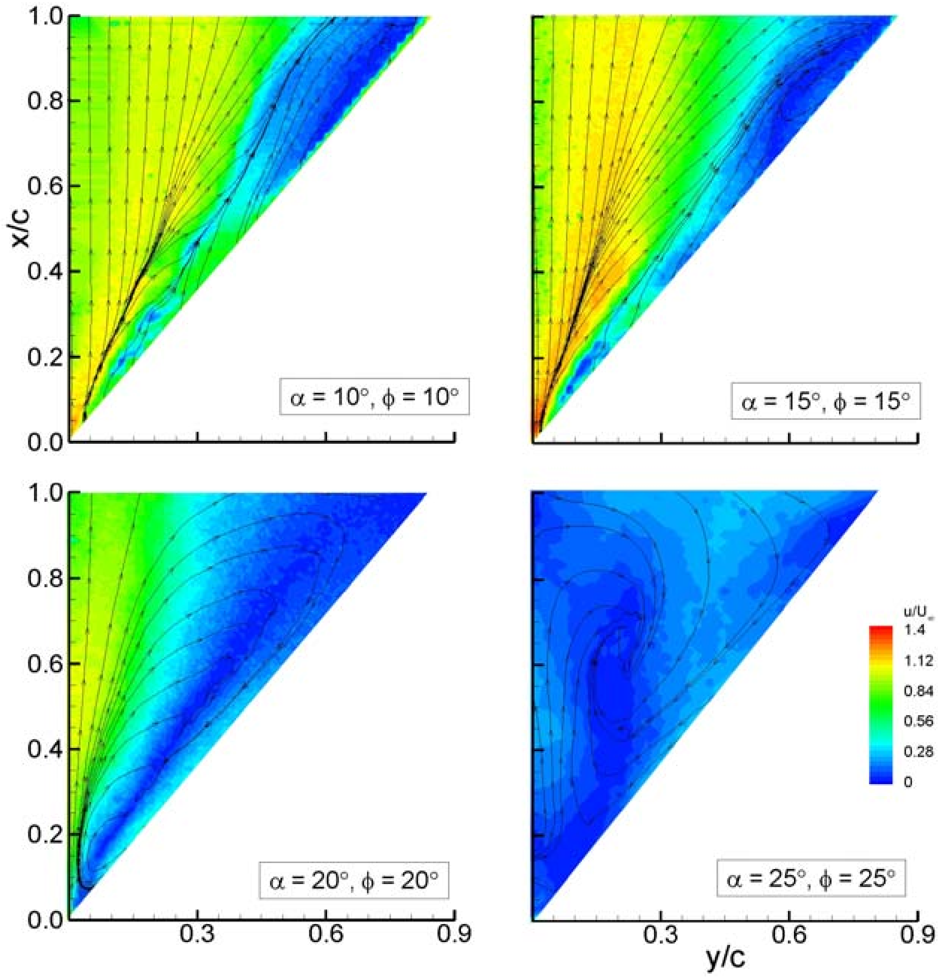

Figure 2.8: Time-averaged velocity magnitude contours and streamlines near the wing surface [12]

2.2 Flow Control Techniques

The definition of flow control is stated as the capability of manipulating, either actively or passively, a flow field to achieve a desired change [32]. Basically, the desire is to satisfy transition delay, increase lift, decrease drag, diminish noise and postpone separation [32]. Flow control on delta wings particularly focuses on eradicating or postponing the vortex breakdown, flow separation and stall; furthermore, recovering the vortical structure and flow reattachment. Various studies were performed in the literature regarding the flow manipulation on both slender and nonslender delta wings and an extensive review of that is present in study of Gursul et al. [5]. In another paper, Mitchel and Delery reviewed the literature in the aspect of delaying vortex breakdown [25]. Among plenty of flow control methods, ones require energy input to the domain are called active control techniques and the rest is named as passive control techniques. Blowing and suction through the passages around the wing, controllable moving flaps, small and high frequency excitation, and plasma actuators are some examples of active flow control techniques [5]. Whereas, since the passive techniques do not require energy input, they appear mostly as geometrical or material changes such as; leading edge, trailing edge or control surface modifications and elastic material to model biomimicry. [33–37].

2.2.1 Active Flow Control

Active control of vortex dominated flow over slender and nonslender delta wings are applied mainly using pneumatic methods for suction and blowing, moving control surfaces, and jet applications through the wing surfaces. One of the first research carried out to enhance vortical flow structure using leading edge blowing is performed by Bradley and Wrayt [38]. Wood and Roberts, using the method of tangential leading edge blowing on a slender delta wing, showed that vortex burst can substantially be delayed and aerodynamic performance of the wing can be enhanced [39]. Leading edge blowing is applied to highly swept delta wing at high incidences to control burst or unburst vortices or enhance the flow field in other various studies [39–41]. Gu et al. carried out a study using steady suction and blowing, and alternate suction-blowing at the leading edge and proved that even at the fully stall condition method can successfully recover the coherent vortices over the plan-forms [42]. Moreover, among three methods, the performance of alternated suction-blowing is reported to be most beneficial to retard the vortex burst location. Another unsteady blowing from leading edge of a slender delta wing study showed that blowing frequency selected based on the helical mode instability associated with the vortex breakdown achieves the delay of vortex breakdown location [43]. The effect of oscillatory blowing on a delta wing with a sweep angle of $\Lambda = 50°$ is examined in the study of Williams et al. [44]. Results demonstrated that stall is significantly postponed and development of vortex flow pattern is observed. Steady and decreasing blowing from the leading edge of a non-slender delta wing is also studied in the literature, and presented a significant improvement in the flow field [28]. Another study on 45 degree swept delta wings approved the enhacement of the flow field under the application of steady and unsteady blowing from the leading edge [45]. A combination of leading edge flap and intermittent trailing edge blowing is introduced on a slender delta wing by Vorobieff and Rockwell and findings of the experiments proved intermittent blowing is efficient to delay the vortex breakdown [46]. Yavuz and Rockwell implemented the steady trailing edge blowing on a 35 degree delta wing and achieved the eradication of three-dimensional separation at high incidences [47]. The effect of unsteady blowing in the vicinity of trailing edge of both slender and nonslender delta wing is also discussed in terms of time response of the flow structure to the unsteady blowing in the literature [48]. Apart from the edges, suction and blowing is implemented on the wings along the spanwise direction in various studies. Johari et al. examined the effect of spanwise steady blowing with the experiments performed in water tunnel [49]. It is realized that, while the blowing from a point upstream of the vortex burst position promoted the breakdown, blowing from downstream of that moves the location towards the trailing edge. Various other studies succeed in delaying the vortex breakdown location over slender wings using the core blowing method are present in the literature [50–52]. Trailing edge jets are also capable of delaying the vortex breakdown and satisfying flow reattachment at high attack angles for slender wings, moreover, these jets succeed in enhancing the lift, reattachment of flow and delaying the vortex breakdown near the stall angles for nonslender delta wings as well. [53, 54]. Suction over the wing from particular points are also discussed in the literature and it is shown that both unsteady and steady suction can be effective in delaying the vortex breakdown location significantly [55, 56]. Especially in the study of Badran et al. suction almost doubled the spanwise position of the vortex breakdown location, which can be seen in Figure 2.9 [57]. Flaps are utilized in the enhancement of car and airfoil aerodynamics. There are also studies where flaps are used as an active flow control mechanism. Oscillating leading edge flaps are introduced by Deng and Gursul to a slender delta wing to examine leading edge vortices and vortex burst. Findings showed that oscillation amplitude is important in the control of the vortex burst location, moreover, oscillating flaps are efficient only if the vortex breakdown location is close to the trailing edge, otherwise the adverse pressure gradient becomes dominant [58]. Lift enhancement with the cost of increase in drag is also shown to be possible utilizing the gurney flaps on nonslender delta wings in the literature [59].

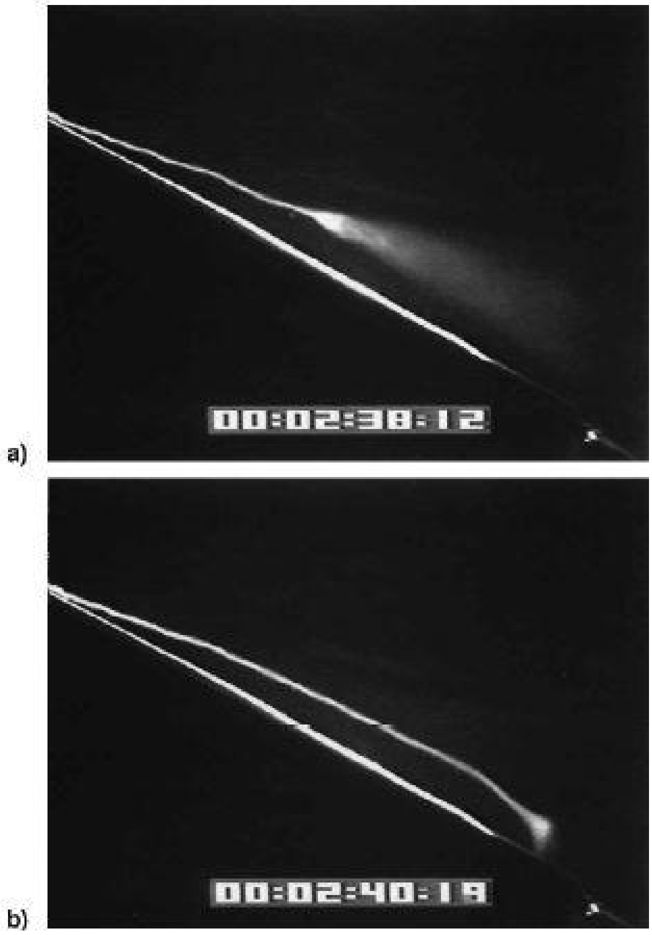

Figure 2.9: Flow visualization of retarding the vortex burst location due to the suction at the trailing edge [57]

2.2.2 Passive Flow Control

Passive flow control techniques, on the contrary to the active ones, do not require any energy input. Accordingly, they are far easier to apply, yet, might cause undesirable impacts at certain flow or flight conditions. The primary difference between geometries of delta wings is the sweep angle that defines whether the wing is slender or nonslender. The extensive research of sweep angle effect started at 1966 [7]. In another study, wing with a varible sweep angle mechanism is utilized to understand the effect of sweep angle to the position of vortex breakdown [60], despite changing a geometrical parameter might be assumed as an active flow control technique. Aerodynamic performance of flexible delta wings with various sweep angles from 25° to 65° are investigated with force measurements and oil flow visualization [61]. Study demostrated the effect of sweep angle to the lift coefficient, which is shown in Figures 2.10 and 2.11, and the maximum C_L value appeared as higher in flexible wings than in rigid ones for Λ = 30° - 50° sweep angles. Although, for the other wings, maximum lift coefficient is higher in rigid ones and they experience the stall at higher incidences. Self-excited flexible wings with sweep angle of 40° - 60° are examined and the results showed significant amelioration in the lift coefficient and stall angle for the nonslender ones with sweep angle of which is less than 60° [33]. Leading edge modifications emerge as another passive control method implemented in the literature. Effect of leading edge bevel angle on aerodynamics of low swept delta wing is studied by Wang and Lu and they stated that leeward bevel angle enhanced the stall angle and the maximum lift over the wings while at very low attack angles, leeward beveled wings might experience negative lift [62]. Bio-inspired leading edge modifications are studied in order to alter the flow topology [63, 64]. Chen and Wang examined vortex structure around low swept delta wing with sinusoidal leading edge modification, inspired from humpback whales, in the study where the bio-inspired wings retard the delay [64]. Enhancement of flow structure of low swept delta wings with sinusoidal leading edge modification are also observed in various other studies [65, 66]. In one of the very recent study, delta wing with sweep angle of 45 degree are slotted, with the inspiration by the nature, hence, an improvement in the stall angle is observed [67].

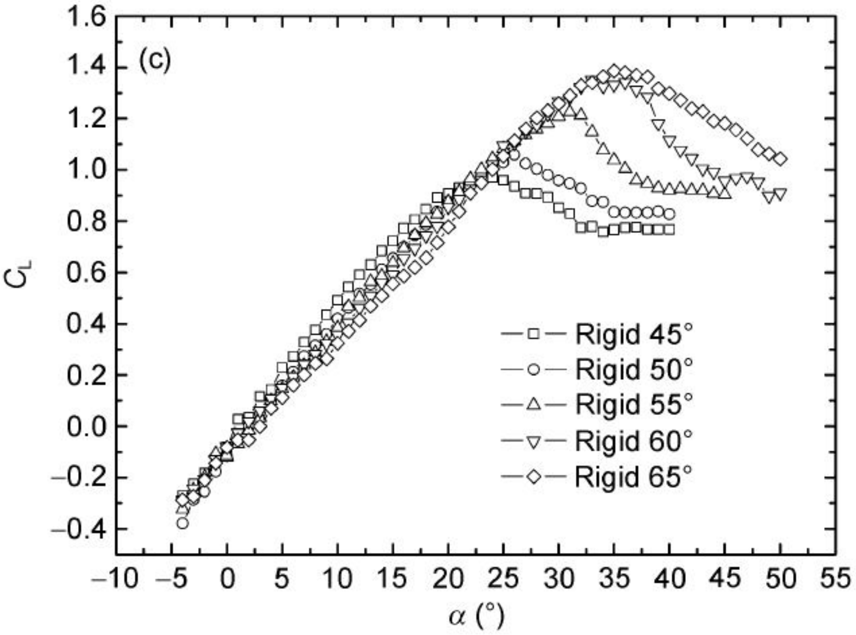

Figure 2.10: Comparison of lift coefficients of delta wings with different sweep angles [61]

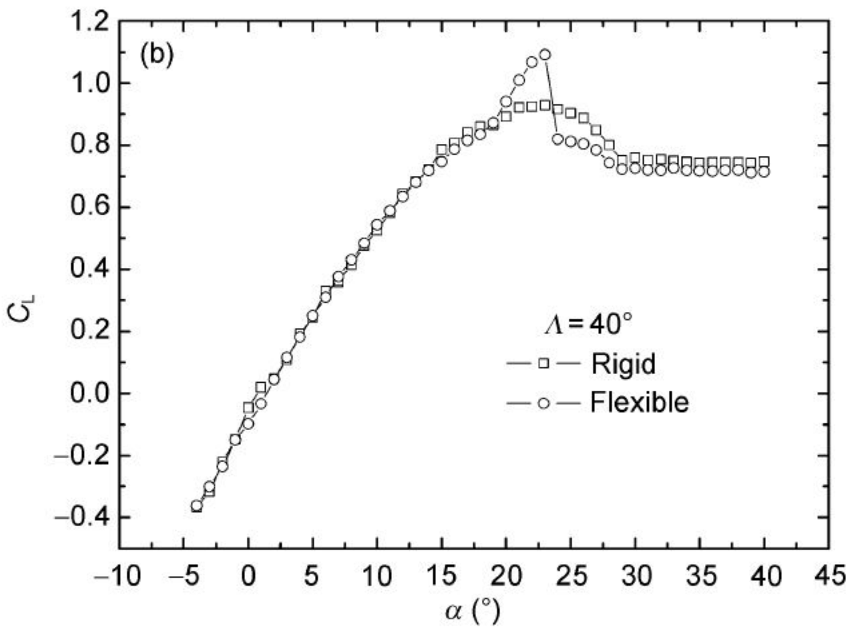

Figure 2.11: Comparison of the lift coefficients of rigid and flexible delta wings [61]

2.2.2.1 Bleeding

As it is mentioned in the introduction chapter, bleeding is a control mechanism, either active or passive, that aims to introduce additional momentum to the region where the adverse pressure gradient is dominant enough to cause the separation. This momentum transfer inside the flow medium is achieved due to the inherent pressure difference between high pressure and the low pressure side of the surfaces via passages or holes over the solid structure. The idea behind is almost the same as the blowing and jet injection despite the fact that transferred momentum rate might not be controllable in bleeding. Simple illustration of bleed mechanism over an airfoil is shown in Figure 1.7, noting that in this figure bleed mechanism is utilized in the way of triggering the turbulence transition in order to retard the flow separation over an airfoil. Bleeding can be applied passively, which is relatively easier to apply compared to active ones, or actively by manipulating the bleed passage geometry into the desired shape/orientation. The very first study where the bleeding is applied on slotted wings and ailerons is reported by Lachmann in 1924 [68]. Passive porosity is stated to have a potential to be utilized as a flow controller [69–71]. In the experimental study carried out by Kearney and Glezer of active bleeding at wide range of angles of attack from pre-stall to post-stall condition, improvement in the aerodynamic forces is observered [15]. Çelik et al. published an experimental study that demonstrates the effect of passive bleed on a nonslender delta wings [16]. In their study, three different bleed orientation, named as Back (B), Edge (E), and Back-Edge (BE), are implemented on a delta wing with sweep angle of 45 degree, and results exhibit that the efficacy of Back bleed orientation in the elimination of three dimensional separation is superior to other bleed orientations. The flow reattachment is achieved at the pre-stall region with the use of passive bleed method on nonslender delta wings. Passive bleeding is also applied to the 45 degree swept delta wings and wings with three different Back angle configurations are studied in the literature [17]. Findings of the study showed that among three wings with three different bleeding configuration angles that are 13, 18 and 23 degrees, the wing with 23 degree Back angle configuration demonstrated the best performance in terms of flow reattachment. These outcomes regarding the effect of passive bleeding on nonslender delta wings are positive, yet there are various points to discuss.

CHAPTER 3

EXPERIMENTAL SET-UP AND MEASUREMENT TECHNIQUES

In this chapter, the details of the experimental set-up and the measurement techniques including surface pressure measurement, particle image velocimetry and force measurement are given.

3.1 Wind Tunnel

The study is carried out in the wind tunnel located in the Fluid Mechanics Laboratory of Mechanical Engineering Department of Middle East Technical University. The type of the wind tunnel is a low-speed, suction-type, and open circuit and it is fed by an axial fan with 10kW AC motor.

The wind tunnel has two symmetric air intakes where fine mesh screens are situated in order to prevent the undesired particles and satisfy the uniformity of the flow. Air enters the tunnel through these inlets and faces with three more fine mesh screens and one flow straightener to further decrease the turbulence intensity at the settling chamber which is 2700 mm long. Afterward, air passes through the contraction part with 2000 mm length and contraction ratio of 8:1. The test section with the dimensions of 750 mm width, 510 mm depth and 2000 mm length follows the contraction part. Walls of the test section is made up of plexiglass; hence, it becomes transparent in order to utilize the optical flow measurement methods. At the end of the test section, diverging duct with the length of 7300 mm is followed by the fan. This structure of the wind tunnel with five distinct parts are designed to achieve a flow with a maximum speed of 30 m/s, turbulence intensity less than 1%, and the blockage ratio below 2.9% at the maximum angle of attack α = 36° over the entire experimental matrix.

The picture of the facility and the test section are shown in Figure 3.1.

Figure 3.1: Picture of METU Mechanical Engineering Department wind tunnel (above) and test section (below)

Despite that the maximum tunnel speed is 30 m/s, the maximum operational speed is around 15 m/s due to the safety concerns. Experiments were conducted at two free stream velocities which are U_∞ = 5.63 and 11.36 m/s. Therefore, the corresponding Reynolds number calculated based on the chord length, C, in Equation (3.1) appear as Re = 5.0 x 10^4 and 1 x 10^5.

$$Re = \frac{U_\infty C}{\nu} \tag{3.1}$$

Wings were tested at the center of the test section with a mounting mechanism that is placed on top of the test section. A robust thin strut invulnerable to the vibrations that might occur due to the air flow suspends the wings at the desired position. The angle of attack, α, of the wing is arranged with respect to the free stream velocity with a rotating mechanism inside the mount. The representation of the mount on top of the test section is displayed in Figure 3.2.

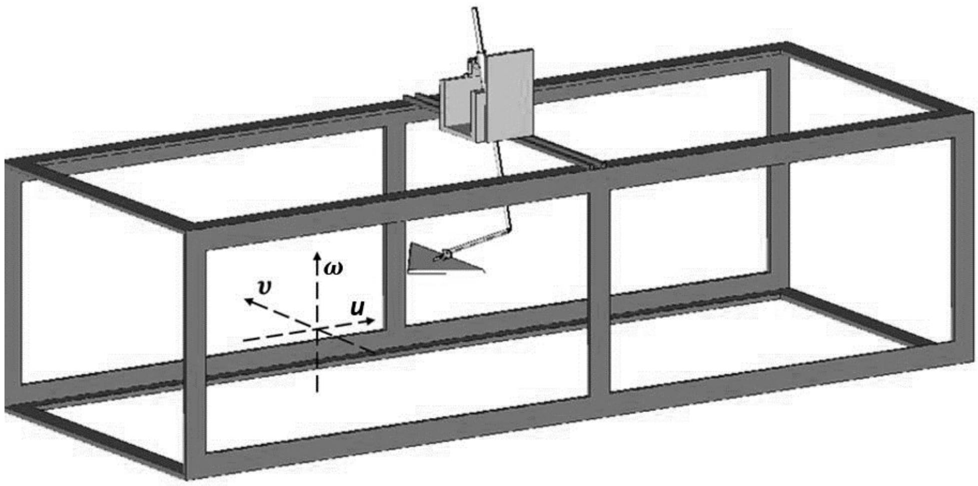

Figure 3.2: Sketch of the wing suspended in the test section

The tunnel characterization was performed by the previous lab members and stated in the thesis of Zharfa that velocity measurements performed with both Laser Doppler Anemometry and Pitot-static tube with both inclined manometer and piezoelectric pressure scanner [72]. As it is reported, measurements done at different tunnel speed by traversing the measurement volume of the LDA along the center line of the test section to acquire the free stream velocity as well as the pitot-static tube. The high temporal and spatial resolution of LDA, moreover, results in the acquisition of the turbulence intensity at distinct fan power levels. Free stream speeds at the same points in the test section are also obtained using the pitot-static tube. Comparison between the tunnel speed results points out to a maximum difference of 3% approximately. Maximum turbulence intensity in the test section is also reported to be around 0.9%, as it is indicated in Figure 3.3 with the tunnel characterization curve.

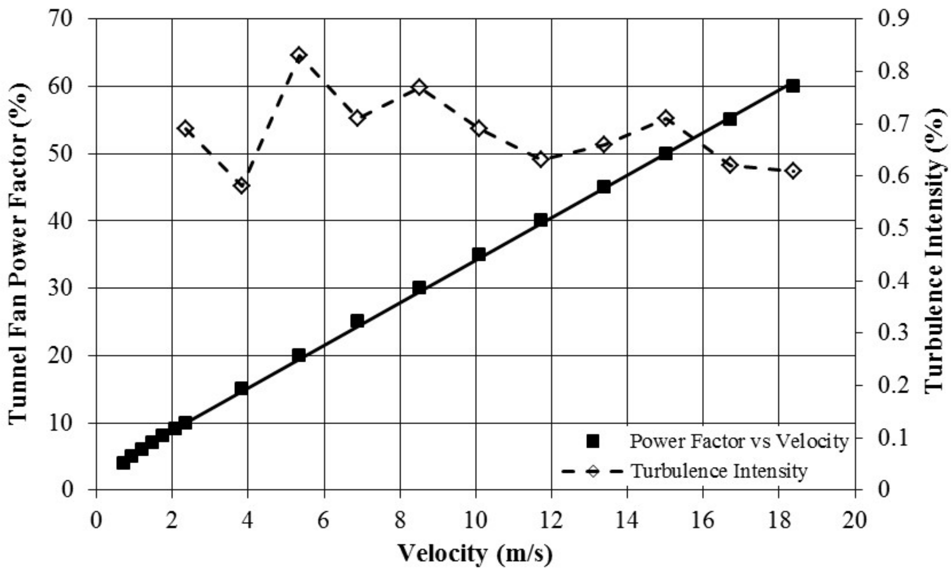

Figure 3.3: Graph of wind tunnel characterization and turbulence intensity [72]

3.2 Wing Models

Four plan-forms with the passive bleeding channels and the Base wing are used in the study to investigate the effect of bleed opening ratio, bor. The wings are produced at the METU BİLTİR Center by employing the rapid prototyping technique. Rapid prototyping is an additive manufacturing method that bonds the particles of fine polyamide PA2200 layers with thickness of 0.15 mm with respect to the 3-D sketch provided by a CAD file. Thus, the maximum roughness level at any surface of the wing is 0.15 mm, which has utmost importance in order to minimize effects of surface impurities to the flow field.

On a delta wing, chord, C, is defined as the minimum distance between the apex and the trailing edge and span, S, is defined as the maximum distance between leading edges. In this study, thickness, span, chord, and the sweep angle are the same for all wings and selected as 8 mm, 270 mm, 135 mm, and 45 degree, respectively. Both suction and pressure side of the Base wing are presented in Figure 3.4 with the pressure measurement holes and the span and the chord are denoted by the S and C, respectively. Base wing is lack of bleeding passage and utilized as a reference wing.

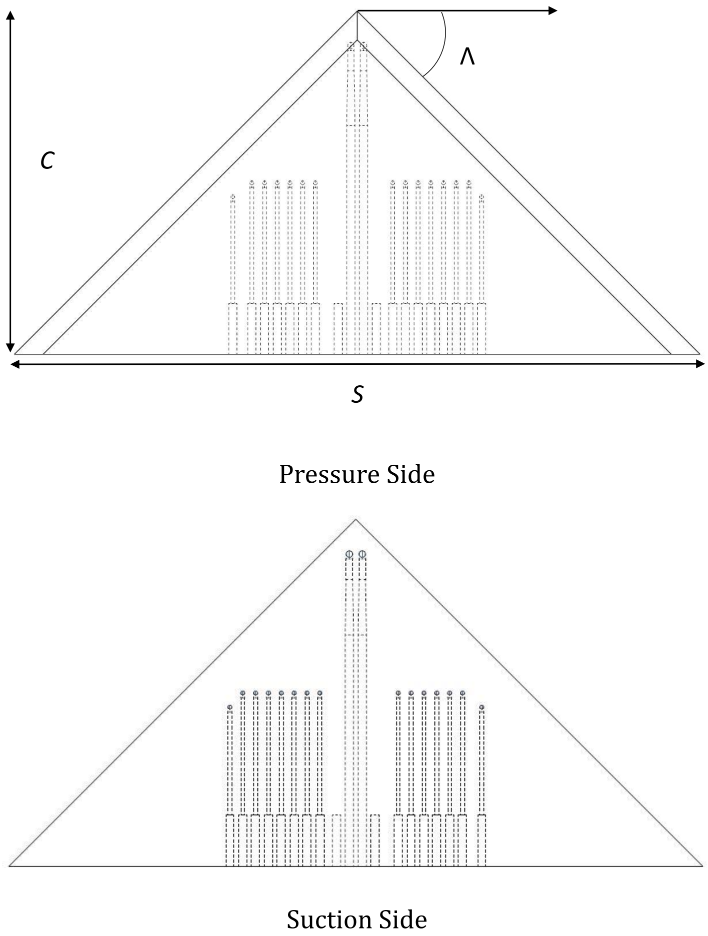

Figure 3.4: Sketch of the pressure and suction side of the base wing with the pressure taps

Çelik et al. [63] defined three different angles over the 45 degree sweep angle wings and opened bleed channels with respect to these angles, defined as Back (B), Edge (E), and Back-Edge (BE). In the study of Çelik et al., it is proved that bleed orientation, named as Back, enhanced the flow field the most and achieved the flow reattachment up to certain angles of attack. Accordingly, in the present study, the examination of effect of the bleed opening ratio was carried out for the bleeding orientation of Back angle, defined in the related article. In Figure 3.5, the sketch on top shows the local coordinate system to define the Back angle which is lying on the *x'-y' plane* where the *x'-axis* is on the wing surface and parallel to the leading edge and *y'-axis* is normal to the wing surface. Bleed angle, in other words Back angle, is defined with θ and taken to be 23°. In the same figure below, the suction side of four wings is shown with the details of the bleed passages. The four wings are named with respect to the bleed opening ratio that is defined as the ratio of the area of the bleed passage of the corresponding wing to that of the wing with the maximum bleed opening. The fully open delta wing with bleed opening length, l, of 121 mm is named *bor* = 1.00. The other three wings with l = 21, 15, 9 are named as *bor* = 0.85, 0.60, 0.35 respectively. The detail in Figure 3.5 demonstrates, r, as the radius of the curvature of the holes and, p, as the distance between the leading edge and the channels at the suction side.

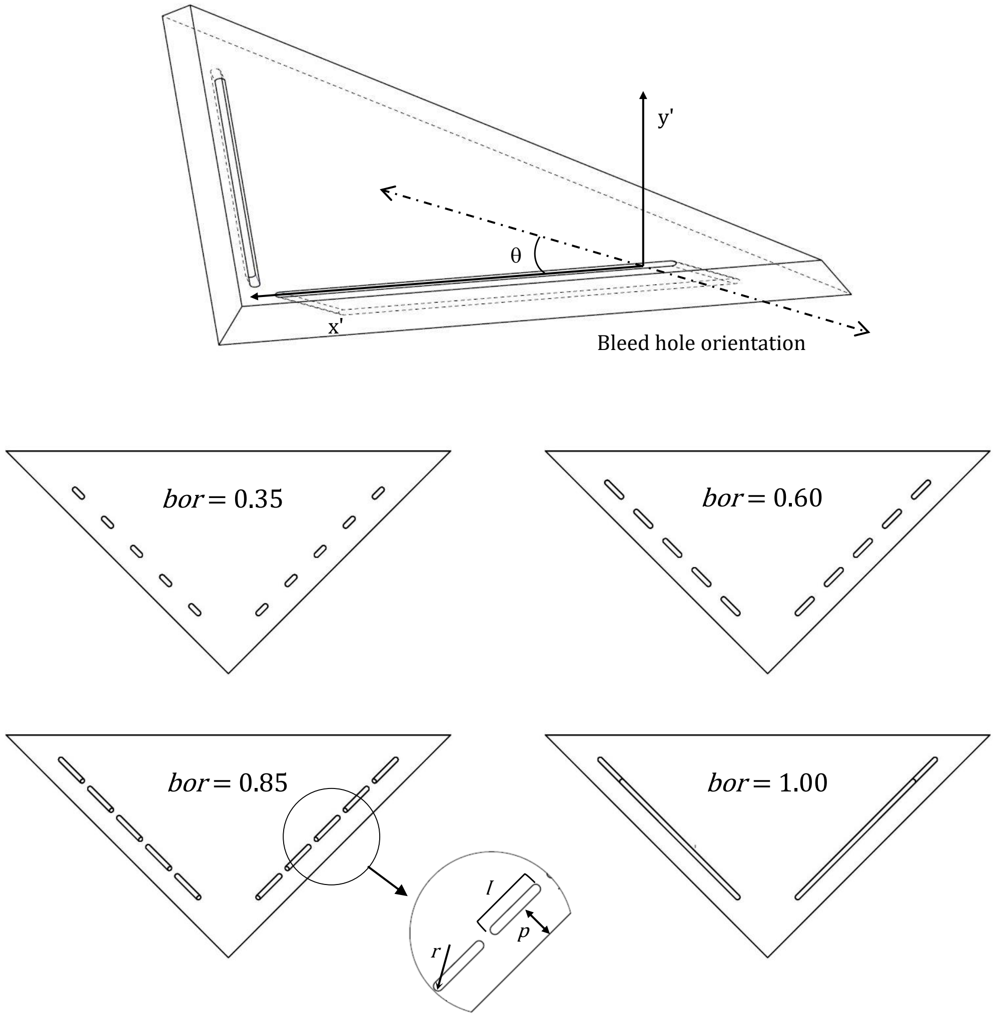

	l (mm)	r (mm)	p (mm)	θ
$bor = 1.00$	121	1.5	11.5	23°
$bor = 0.85$	21	1.5	11.5	23°
$bor = 0.60$	15	1.5	11.5	23°
$bor = 0.35$	9	1.5	11.5	23°

Figure 3.5: Sketch of the plan-forms showing the details of the bleed orientation and bleed openings

Figure 3.4 demonstrates the span and chord on the Base wing. Furthermore, in the same figure, pressure taps and the smoke holes are displayed with the dashed lines, although the smoke visualization was not performed during the study. The pressure measurement location is defined at the chordwise non-dimensional position of x/C

= 0.5 at the suction side of the wings. While the Base wing has 19 pressure taps in total, due to the presence of the bleed passages, other four wings have 13 taps. The positions of the pressure taps are located at the non-dimensional spanwise locations of y/s = 0.21, 0.28, 0.36, 0.43, 0.50, 0.58, 0.65, 0.73, 0.80, 0.87, noting that the length of s is equal to the quarter of the length of the span, S. Figure 3.6 exhibits the pictures of the five wings tested in the study. The surfaces of the suction side of the plan-forms are painted with black color in order to overcome reflection problem during the PIV application.

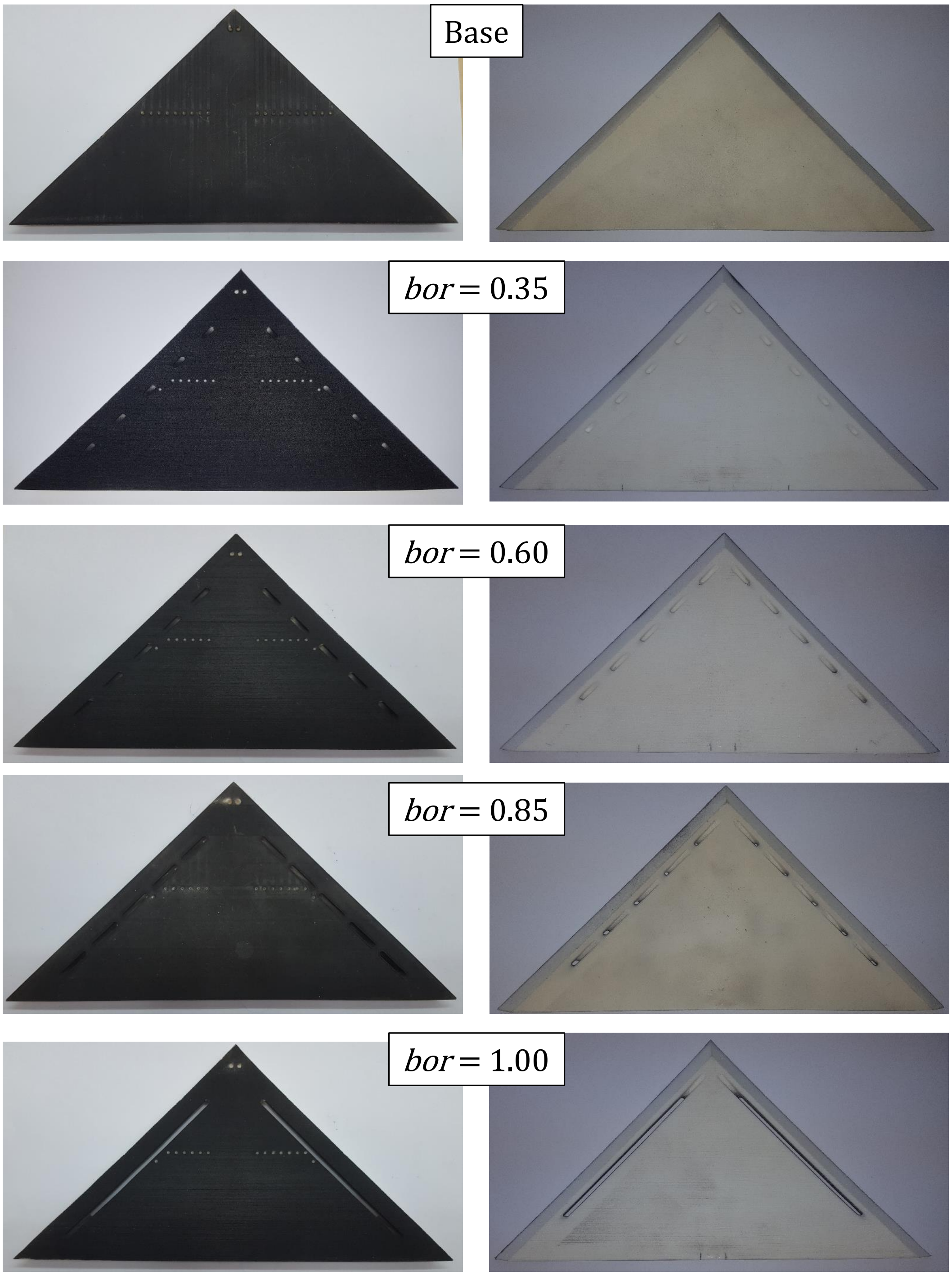

Figure 3.6: Pictures of the manufactured wings used in the present study

3.3 Measurement Techniques

The investigation is carried out employing three measurements methods namely, surface pressure measurement, particle image velocimetry (PIV), and force measurement.

3.3.1 Surface Pressure Measurement

Steady-state pressure measurements were performed using Netscanner 9116 Intelligent Pressure Scanner which has 16 silicon piezo-resistive pressure transducers. Pressure scanner is capable of recording data at 500 Hz, and the range of the sensor is limited to 0 - 2.5 kPa. Despite that the manufacturer provides the pre-calibration for certain pressure and temperature ranges, validity is confirmed with manometer readings as well. Pressure scanner can carry out the measurements with a resolution of $\pm$ 0.003% FS (full scale) and accuracy of $\pm$ 0.05% FS when the combined errors due to non-linearity, hysteresis and non-repeatability are taken into consideration.

Preliminary experiments demonstrated that two sets of 5000 data sample, acquired at 500 Hz, is enough to satisfy the saturation of the results and further repetitions do not alter the results significantly. Therefore, average pressure measurements were recorded at 500 Hz for three sets of 5000 samples, rather than two sets to re-ensure the saturation. External noise was also acquired before each experiment case at the same sampling rate, and the average of that was subtracted from the average of the pressure measurements. This noise is mainly generated by the wind tunnel fan, the wind tunnel fan control unit and all other electronic devices, and it is assumed to be steady-state or periodic.

Since the measurements were done in the suction side of the wings, the pressure, which is gauge, appears as negative. Therefore, non-dimensional pressure coefficient C_p is demonstrated as $-C_p$ in the charts. Pressure coefficient, C_p, is calculated with the following Equation 3.2:

$$C_p = \frac{\overline{p} - p_\infty}{\frac{1}{2}\rho U_\infty^2} = \frac{\overline{p} - p_\infty}{p_{dyn}} \tag{3.2}$$

3.3.2 Particle Image Velocimetry (PIV)

Particle Image Velocimetry (PIV) is a state-of-art flow measurement technique which is employed in a substantial portion of this study. The technique is a quantitative, non-intrusive optical flow measurement method that provides instantaneous velocity field either in 2D or 3D domain, depending on the type of the PIV. During the study, Planar PIV is employed to extract the two velocity component u and v within the plane in the vicinity of the wing suction surface. The fundamental logic behind the PIV is to trace the seeding particles by taking two subsequent picture of the flow field that is illuminated by the continuous laser sheet. Images are divided into the smaller regions that are called interrogation area (IA). Positions of the particles are compared in image-1 and image-2, and for each IA, an average displacement vector is estimated. As the time difference between the two successive images, Δt, is known as a user-defined input, the average velocity vector is calculated by dividing the average displacement of the particles to the time step for each IA, therefore, the whole flow field can be obtained.

Flow measurement experiments were carried out by using TSI PIV hardware and Insight4G software in order to acquire the data acquisition and for further processes. The laser of the system is a dual-pulsed Q-switched Litron Nano L200-15 200mJ Nd:YAG. Laser beam passing through a cylindrical lens with a radius of -15 mm and spherical lens with a focal point of 1000 mm, respectively, is converted into a laser sheet. This combination of lenses is selected considering the maximum velocity within the region of interest in order to ensure maximum displacement of seeding particles inside the laser sheet is less than one-fourth of the length of IA, and to illuminate the domain adequately. Images were taken with a high-speed 4-megapixel CMOS camera and the lens of the camera was Nikon AF NIKKOR 50mm f1.8. The laser shutter speed is limited to the sampling rate of 15 Hz, hence, image pairs were also acquired at the rate of 15 Hz. TSI LaserPulse$^{\text{TM}}$ 610036 synchronizer satisfied the synchronization of camera and laser with respect to the inputs provided by the user via the computer. Focus plane of the camera was aligned with the laser sheet which was kept underneath the wing surface with a distance, Δz, of 2.5 mm with the same angle of attack. The sketch of the alignment of these three elements is explicitly shown in Figure 3.7.

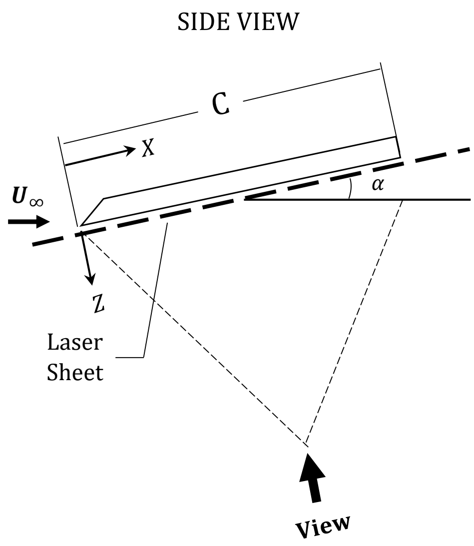

Figure 3.7: Sketch of the near surface PIV experimental set-up

During the experiments, seeding particles, properties of which must be selected appropriately to ensure that they follow the flow stream, were generated through the vaporization of a glycol-based liquid and released into the wind tunnel from a commercial smoke machine. Since the domain of the experiments was air, the size of the particle becomes significant. Particles can follow the air flow stream provided that the diameter of a particle is in the range 0.5 - 5 μm, and that of glycol-based smoke is in 1 - 3 μm [73]. Once the homogenous distribution of seeding particles was achieved, the data acquisition was initiated.

For each case, 200 pairs of image were taken, and these raw images were processed by dividing the region of interest into the 32 x 32 square pixels interrogation windows, which corresponds to the effective grid size of Δ/C = 0.022. Using FFT correlator, cross-correlation between each image pairs were performed to achieve the time-averaged velocity field $\langle V \rangle$. The velocity field, further, was post-processed to obtain time-averaged streamlines ,$\langle \Psi \rangle$, time-averaged non-dimensional vorticity $\langle \omega_z C/U_\infty \rangle$, time-averaged non-dimensional streamwise velocity component $\langle u/U_\infty \rangle$, velocity magnitude root-mean-square V_{rms} in Tecplot Focus.

3.3.3 Force Measurement

Forces present over the plan-forms were measured using ATI-Gamma SI-32-2.5 Force/-Torque (F/T) sensor. The whole acquisition system consists of 4 components which are the F/T transducer, F/T transducer cable to the power supply, DAQ transducer power supply, cable to connect DAQ card to the power supply. The integrated electronic system inside the power supply 9105-C-H-PS-10, was fed by an external electric source of 5V. Raw data was digitized via NI PIC-6024E - 16 channel 12-bit DAQ card. Accuracy of the device provided by the manufacturer is $\pm$ 0.01% FS for the measurement axes that are used in study. The transducer is capable of reading the maximum force of 32 N at a maximum sampling rate of 10 kHz. The manufacturer provides the calibration matrix and the interface developed in Labview. Nevertheless, to assure the calibration, preliminary measurements were performed with both the commercial force transducer and the in-house one, then the obtained results were compared. It appeared that both readings were consistent. The in-house developed force measurement device is an internal force balance and the data obtained through this device is published in the study of Ghazijahani [24].

The wings were suspended inside the tunnel vertically during the force measurements, as in Figure 3.8, whereas it was horizontal for the pressure and PIV measurements. The reason for that is to measure the lift and drag forces on the axes where the device is the most sensitive. Manufacturer reported that the resolution in the z-axis which is the vertical axis is 1/80 N while the resolution value of both x and y axis which are lying in the horizontal plane is 1/160 N. In order to inspect whether vertical placement affect the results, pressure measurements were performed and compared with the same cases in which the wing was suspended horizontally. The difference between the measurements was insignificant. The angle of attack, α, was altered using a stepper motor and stepper motor driver controlled by an Arduino card. Data acquisition was performed at each 1.8° in $0^\circ \geq \alpha \geq 9^\circ$ & $27^\circ \geq \alpha \geq 36^\circ$ and at each 0.9° in $9.9^\circ \geq \alpha \geq 25.2^\circ$ where the stall regime is expected to occur. Preliminary cases showed that 10 seconds of data acquisition at 5 kHz led to the saturation of the readings. Despite the high capacity of data acquisition of the transducer, sampling rate during the experiments was 5 kHz for 12 seconds in order to minimize the data process time.

Noise was also measured under the same conditions and time average of that was subtracted from the time-averaged force measurements. Air stream creates forces over the strut holding the wing, which is sensed by force sensor and embedded in the total force. In order to minimize this effect, forces occur over the bare strut was measured for each angle of attack of the wing at different Reynolds numbers, and these measurements were subtracted from readings for the wings.

Figure 3.8: Pictures of the force measurement set-up, wing inside the test section and motion control unit outside the wind tunnel

Labview software extracts the data in the text files and the raw data was processed using Matlab. Time-averaged force measurements are present as non-dimensional lift, C_L, non-dimensional drag, C_D, and lift-to-drag ratio, C_L/C_D coefficients for Reynolds number of Re = 5.0 x 10^4 and 1 x 10^5 in Appendix B . Equation 3.3 exhibits the calculation of non-dimensional force coefficients. In the calculation area of the wing is denoted by A which is the surface area of the suction side of the Base wing. Due to the different bleed passage sizes, the surface area of each wing slightly changes, nevertheless, since the aim of the study is to control of the flow structure of the Base wing, the area used in the calculations is chosen to be Base area for all wings.

$$C_L, C_D = \frac{F_L, F_D}{\frac{1}{2}\rho {U_\infty}^2 A} \tag{3.3}$$

3.4 Experimental Matrices

Investigation of the effect of bleed opening ratio to the flow field around a non-slender delta wing was carried out by employing three measurement techniques. There are upper and the lower limitations in order to decide the experimental matrix. Pressure measurement at the Reynolds number below Re = 3.5 x 10^4 results in high uncertainty and above Re = 12.5 x 10^4 the tunnel becomes prone to structural vibrations. Accordingly the experimental matrix is selected as it is shown in Figure 3.9. During the pressure measurements, experiments were carried out at Reynolds numbers Re = 5.0 x 10^4 and 1 x 10^5 for angles of attack α = 17°, 18°, 19° & 20°. Because the ultimate aim of the passive control mechanism is to reattach the flow, angles of attack are the ones where the flow around the Base wing is at the onset of separation or fully separated. Pressure readings were conducted for all wings. PIV measurements, on the other hand, were performed at two different angles of attack at Reynolds number Re = 5.0 x 10^4 for selected wings. At attack angle of 18° near-surface PIV measurements were performed for all wings whereas at α = 20° experiments were performed merely for the Base, bor = 1.00 and bor = 0.85 wings. Furthermore, aerodynamic forces existing over the wing was extracted at the Reynolds numbers Re = 5.0 x 10^4 and 1 x 10^5 where angles of attack were in the range of 0° $\geq \alpha \geq$ 36°. The idea behind the decision of the experimental matrix is to maintain the Base wing in pre-stall/stall condition considering the limitations of the tunnel and the measurement devices.

Measurement Method	Reynolds Numbers	Attack Angle, α
Pressure Measurement	• 5.0×10^4 • 10×10^4	17°, 18°,19°,20°
PIV	5.0×10^4	18°,20°
Force Measurement	• 5.0×10^4 • 10×10^4	$0° \leq \alpha \leq 36°$

Figure 3.9: Experimental matrix for all measurement techniques

3.5 Uncertainty Estimates

Experimental research, due to its nature, contains uncertainty and the estimation of which is crucial in order to present the results of the study. Kline and McKlintock [74], defines the uncertainty as "the possible value the error might have" and they mathematically express resultant uncertainty of a quantity, ω_R, with the following equation:

$$\omega_R = [(\omega_{x_1}\frac{\partial R}{\partial x_1})^2 + (\omega_{x_2}\frac{\partial R}{\partial x_2})^2 + ... + (\omega_{x_n}\frac{\partial R}{\partial x_n})^2]^{\frac{1}{2}} \tag{3.4}$$

Uncertainties present in the force measurements and pressure measurements were estimated using the equation 3.4 using the accuracy of the devices provided by the manufacturer. The abovementioned values for the accuracy of the pressure scanner is taken to be 0.05%(FS), noting that FS refers to full-scale, considering the background noise subtraction performed during the pressure measurements and three sets of data acquired to ensure the saturation of the results. The accuracy of the force transducer is 0.01%(FS). Among the various cases, since each pressure tap measures different pressure due to the varying flow dynamics, the uncertainty in the non-dimensional pressure coefficient varies. The average of the minimum, average of the maximum and the total average of the $-C_p$ are found to be 16.2%, 17.3% and 20.5%, respectively, for the measurements at Re = 5.0 x 10^4. Likewise these values at Re = 1 x 10^5 are 3.9%, 5.2% and 4.2%. The maximum standard uncertainty in the non-dimensional aerodynamic force coefficients, considering the thirty incidences of angles of attack for each wing, estimated for the cases at Re = 5.0 x 10^4 and Re = 1 x 10^5 are below 18.0% and 4.4%, respectively and the peak values appear for both Reynolds number in lift-to-drag ratio coefficients.

Standard uncertainties of PIV measurements, on the other hand, were estimated with method called Peak Ratio method, recently developed by Vlachos et al. [75], where ratio of primary to second peak height ratio as the result of cross-correlation of the image pairs are compared to find the resultant uncertainty, independent from the image quality or flow condition. Insight4G provides the standard uncertainty values estimated using Peak Ratio method for the velocity vectors in the flow field and maximum values of that is found to be 10.2% among all PIV cases.

CHAPTER 4

RESULTS AND DISCUSSIONS

This chapter includes findings obtained during the investigation of effect of bleed opening ratio on the flow structure around the non-slender delta wings. Wings with four distinct bleed opening ratios *bor* = 0.35, 0.60, 0.85 & 1.00 and the Base wing were studied. Experiments were conducted in the broad range of angle of attack in the span of $0° \geq \alpha \geq 36°$ at Re = 5.0 x 10^4 and 1 x 10^5.

4.1 Results of Surface Pressure Measurements

Results of the pressure measurements presented as non-dimensional pressure coefficient, $-C_p$, are discussed in this part. Measurements are obtained at the dimensionless chordwise distance of x/C = 0.5 and along the spanwise distance equal to the quarter of the wing span, s, which is also non-dimensionalized as y/s. In Figures 4.1 and 4.2, $-C_p$ distributions are shown for the wings with *bor* = 0.35 0.60 0.85 1.00 & Base wing. The experiments were performed at α = 17°, 18°, 19° & 20° for the Reynolds Number of Re = 5.0 x 10^4 and 1 x 10^5. In the figures, each chart exhibits distinct findings at different angles of attack and Reynolds numbers which are labeled on the charts. As it is discussed in Chapter 3, the negative value of the C_p is displayed, since the measurements were done in the suction part of the wings, where the leading edge vortex exists. The maximum value of the $-C_p$ is the potential location of the time-averaged vortex core provided that it exists. As the $-C_p$ distribution becomes hump-like, where there is a significant difference exists between the highest and lowest points of the curve, it is the proof of reattached flow structure with vortical structure, strength of which increases as the difference between the highest and lowest points rises. On the other hand, the straight distribution of the non-dimensional pressure coefficient demonstrates the footprints of the flow field experiencing the three dimensional separation.

The minimum angle of attack for the pressure measurements is 17 degree at which the Base wing is almost in the pre-stall regime, as can be deduced from the $-C_p$ distribution at the top left chart of Figure 4.1 at Re = 5.0 x 10^4. $-C_p$ distribution of Base wing, represented with the black lines in all charts, is almost flat and the peak point in the line which is the possible location of vortex core is very close to the symmetry line of the wing. The similar trend appears in the wing *bor* = 0.35, hence, the enhancement over the flow field due to the passive bleed is not observed. On the other hand, for the same chart, wing *bor* = 0.60 & 0.85 have the hump-like $-C_p$ distribution, moreover, the location of possible time-averaged vortex core moved outboard of the symmetry line. Furthermore, wing *bor* = 1.00 has the trend line which clearly represents an recovery of the vortical structure. The difference between the maximum and the minimum points of $-C_p$ is the highest in the chart along the line representing the *bor* = 1.00. At the same angle of attack α = 17°, $-C_p$ distribution at Re = 1 x 10^5 reveals a slightly different scenario where the non-dimensional values are higher compared to Re = 5.0 x 10^4 case. Firstly, although the $-C_p$ trend of Base wing is relatively better in this case, vortex structure is still weak considering the discrepancy between the maximum and the minimum points. Furthermore, *bor* = 0.35 wing again exhibits the similar trend with the Base wing. As the Reynolds number increased to 1 x 10^5, *bor* = 0.60 & 0.85 wings show a strong improvement of in the recovery of the leading edge vortex. At Reynolds number Re = 1 x 10^5, the *bor* = 0.60 wing has a hump-like shape and the approximate difference between the peak and the lowest poing of the $-C_p$ of *bor* = 0.60 is 0.48. Likewise, a significant enhancement in the recovery of vortices can be observed in the $-C_p$ curve of the *bor* = 0.85 wing. The difference between the lowest and the highest points of the curve is almost 0.56 and the peak value of that is closest to the leading edges. The maximum $-C_p$ difference is also achieved with the *bor* = 0.85 wing. Plan-form with the highest bleed opening ratio that is *bor* = 1.00 is expected to have lower $-C_p$ values due to the fundamental mechanism of passive bleeding. Nevertheless, $-C_p$ trend line is shifted above others yet the difference of the max-min values is less than that of *bor* = 0.85

wing. Green line representing the *bor* = 0.60 reveals a trend with the characteristics of both *bor* = 0.85 & 1.00 although the bleed opening is least in between these three plan-forms.

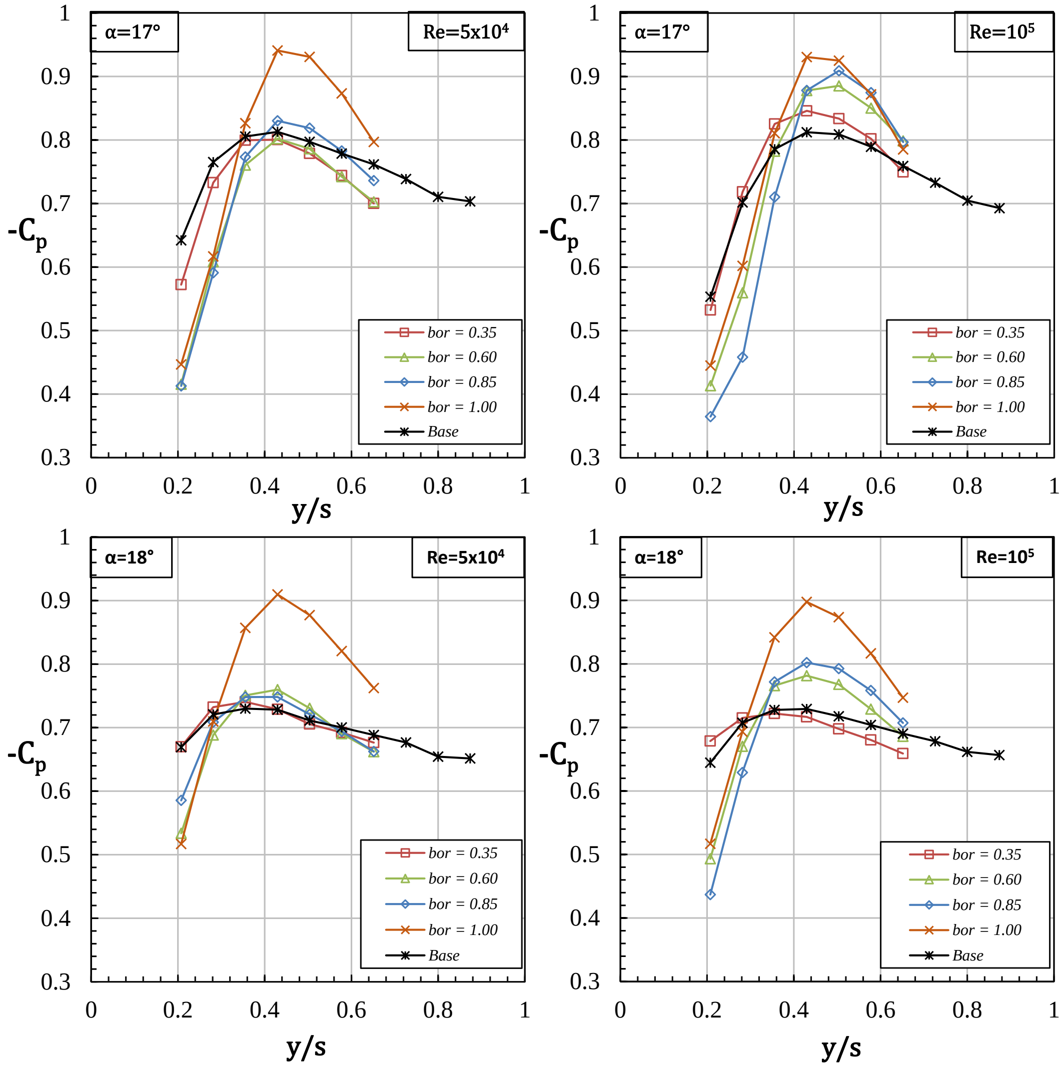

Figure 4.1: Non-dimensional pressure distribution $-C_p$ along the non-dimensional distance of y/s for *bor* = 0.35, 0.60, 0.85, 1.00 & Base wings at Re = 5.0 x 10^4 (left column) and 1 x 10^5 (right column) for α = 17° & 18°

At the rest of the pressure measurement cases, at distinct angles of attack and Reynolds numbers, the $-C_p$ distribution of the Base wing is quite flat, hence, one can deduce that the flow is separated and the wing is in the pre-stall regime. Since the pressure measurements were performed at a cross-section of the wing, the characteristic of the flow field at upstream of the chordwise pressure measurement location cannot be deduced, by solely considering the pressure measurements. Hence expressing that the wing is stalled might be misleading without observing the force measurements results.

In Figure 4.1, bottom left chart demonstrates the non-dimensional pressure coefficient distribution for α = 18° at Re = 5.0 x 10^4. While *bor* = 0.35 and Base plan-forms have straight pressure cofficient distributions, the trend line with a small difference between the min-max $-C_p$ value is observable for *bor* = 0.60 & 0.85. On the other hand, fully opened wing, *bor* = 1.00 still keeps the hump-like shape in the $-C_p$ distribution. Considering the difference of minimum and maximum points along the curve of $-C_p$, *bor* = 0.60 wing displayed improved performance in the enhancement of the flow structure compared to the *bor* = 0.85, albeit that the enhancement is insignificant and might be a reading error. As in the previous case, it is observed that the increase in the Reynolds number to the Re = 1 x 10^5 leads the *bor* = 0.60 & 0.85 wings excite the flow field effectively in order to achieve a significant change. The positions of peak of $-C_p$ are approximately at the same region for *bor* = 0.60, 0.85 & 1.00 wings at angle of attack of α = 18°. While the difference in between the maximum and minimum points of $-C_p$ appear to be almost the same for *bor* = 0.85 & 1.00 wings, in terms of that *bor* = 0.60 revealed the least effective performance among these three. Again, the $-C_p$ distribution of *bor* = 1.00 is shifted above compared to the *bor* = 0.85, which is not expected.

Experiments performed at α = 19° and 20° at Reynolds number Re = 5.0 x 10^4 and 1 x 10^5 are demonstrated in the graphs of Figure 4.2. All plan-forms except for *bor* = 1.00 are lack of the hump-like structure of $-C_p$ curve and it can be expressed that they experience the three dimensional separation and are in the pre-stall regime. However, trend of the $-C_p$ curve of *bor* = 1.00 is still in hump-like shape even at the attack angle of 20°, despite that the vortex is not very strong considering the difference between the maximum and the minimum value of the $-C_p$. Nevertheless, the vortical structure that is completely lost over the Base wing is recovered by the bleeding and fully opened wing is capable of doing so even at the extremities as such angles of attack. Two details that is not easy to take notice for *bor* = 1.00 wing appear for all cases. One of which is that trends show that the $-C_p$ values are roughly the same for both Reynolds numbers at each case, hence, the control of the flow field with fully opened wing may be Reynolds independent, which is one of the very first feature for a passive flow control method is expected to have. The second detail, on the other hand, is the peak point of the $-C_p$ which is the potential location of the time-averaged vortex core is found to be at the same non-dimensional spanwise location where y/s is equal to 0.43, although this might not be an important feature for the flow field or flight stability which is the ultimate aim of flow control techniques, the reason behind this is vague.

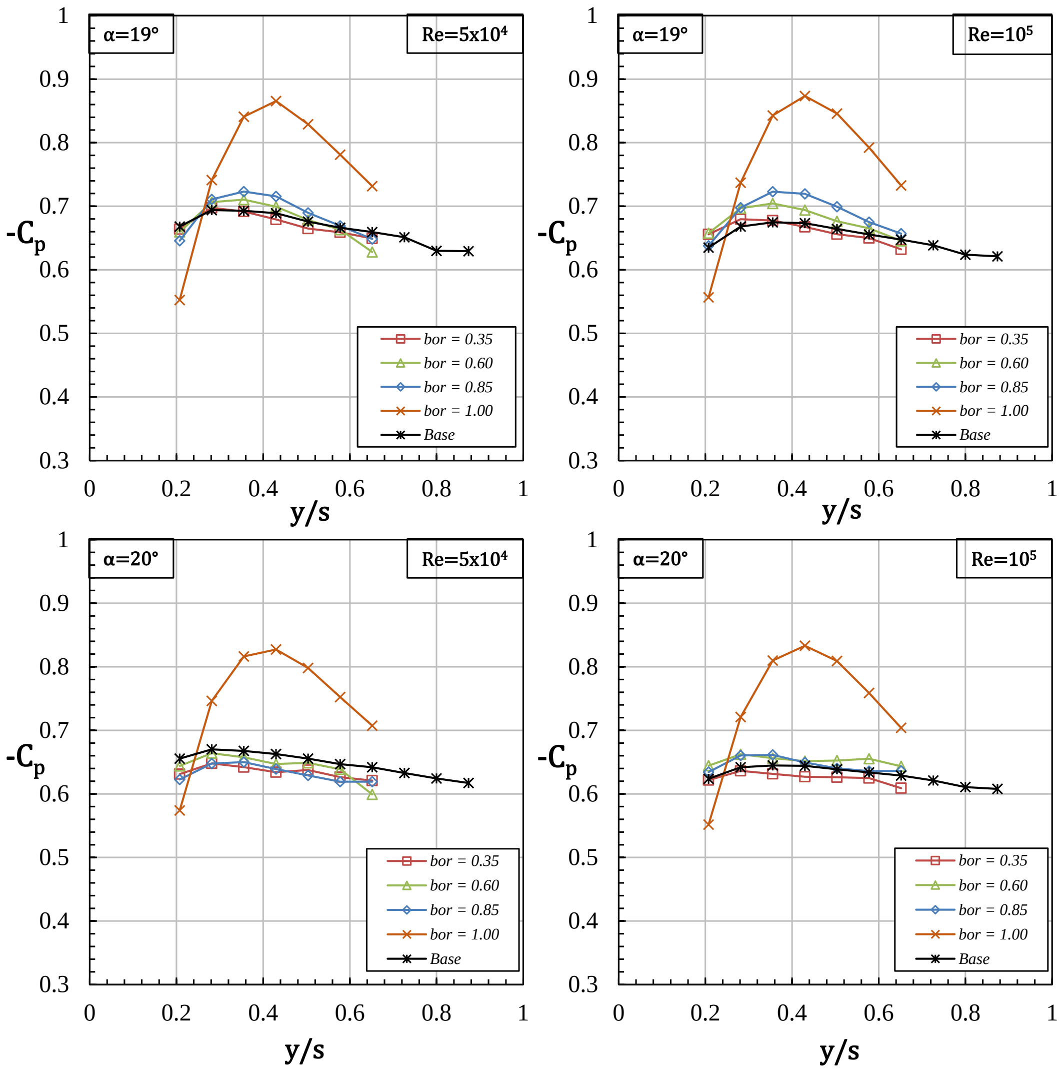

Figure 4.2: Non-dimensional pressure distribution $-C_p$ along the non-dimensional distance of y/s for *bor* = 0.35, 0.60, 0.85, 1.00 & Base wings at Re = 5.0 x 10^4 (left column) and 1 x 10^5 (right column) for α = 19° & 20°

The minimum point of the $-C_p$ is accepted to be the reattachment line for a continuous measurement along a line from symmetry line to the leading edge. However, due to the geometrical constraints in the design of the wing models, the number, accordingly, the location of the pressure taps are restricted. Results show that the minimum points is always take its place at the very first pressure tap, hence, stating that this location is the reattachment point might be a misleading conclusion. Although the hump-like $-C_p$ distribution is the foot-print of the flow reattachment to the wing surface, the point of reattachment is not clear with respect to the available pressure measurement findings. The results of pressure measurements in general are in line with the study of Çelik et al. [16] where the passive bleeding with the Back angle orientation is capable of recovering the vortical structure and of reattaching the flow to the plan-forms. Present data also shows that increase in the bleed opening ratio leads the passive bleeding function for the further angles of attack, in other words, various flight conditions.

4.2 Results of Surface PIV Measurements

PIV experiments were carried out for the Re = 5.0 x 10^4 at attack angle α = 18° for all wings. Based on the results obtained at α = 18°, PIV measurements were also conducted at the Re = 5.0 x 10^4 for the angle of attack of 20 degree only for the *bor* = 0.85, 1.00 & Base wings. Particle image velocimetry measurements were performed at the plane in the vicinity of the wing suction surface and the obtained velocity field $\langle V \rangle$, constant contours of non-dimensional vorticity $\langle \omega_z C/U_\infty \rangle$, streamlines $\langle \Psi \rangle$, constant contours of non-dimensional streamwise velocity component $\langle u/U_\infty \rangle$ and constant contours of velocity magnitude root-mean-square V_{rms}, all of which except for V_{rms} are time-averaged, are demonstrated and discussed. Solid lines in the constant time-averaged non-dimensional vorticity contours represents the positive values while the dashed lines stands for the negative contours. For all cases, the absolute minimum and the absolute incremental values for each contour are the same and stated in the caption of each figure. The symbols of the vertical (streamwise) and horizontal (spanwise) components of the velocity fields are presented with the letters u and v, respectively. Non-dimensional constant streamwise velocity component contours are shown with the shaded regions which present the u velocity component, direction of which are opposite to the direction of the free stream velocity. In each PIV result, a triangle representing the position of the half of the plan-form is inserted to the pictures. The data acquisition was performed for the region approximately to two third of the plan-form area to confirm the symmetry of the flow field and and it was repeated for half of the wing to increase the resolution, therefore, results of the half wings are shown.

In Figure 4.3 data obtained for the Base wing at angle of attack of α = 18 at Re = 5.0 x 10^4 is demonstrated. The PIV measurment results are mirrored to resemble the whole wing surface. The top left figure showing the velocity field of the Base wing reveals the sudden drop of the magnitudes of the velocity vectors at the downstream of the leading edge. The streamlines demonstrated at the top right figure has a pattern with a large-scale, inward-swirling surface streamline, that is the main foot-print of the three-dimensional separation that is stated in Chapter 3. The non-dimensional vorticity contours elongated from apex to the center of the wing which is the indication of vortex dominated and reattached flow structure does not exist in the dimensionless vorticity contours at the bottom left data of Figure 4.3. These three findings indicate that for the Reynolds number of 5.0 x 10^4 at angle of attack α = 18°, the Base wing experiences the three-dimensional separation and it is inline with the outcomes of the pressure measurements. At the bottom right picture of the Figure 4.3, the negative streamwise velocity component contours are shown with the shaded area. The magnitude of the streamwise velocity component opposite to the free stream velocity increases near the leading edge due to the existence of the bifurcation line. Furthermore, roughly two third of the wing is dominated by the reverse flow and elimination of this might eradicate the three-dimensional separation by suppressing the effect of adverse pressure gradient and reattach the flow to the wing surface. The comparison of the four wings with different bleed opening ratios are made in the further discussion having in mind that the Base wing has already experienced the three-dimensional separation.

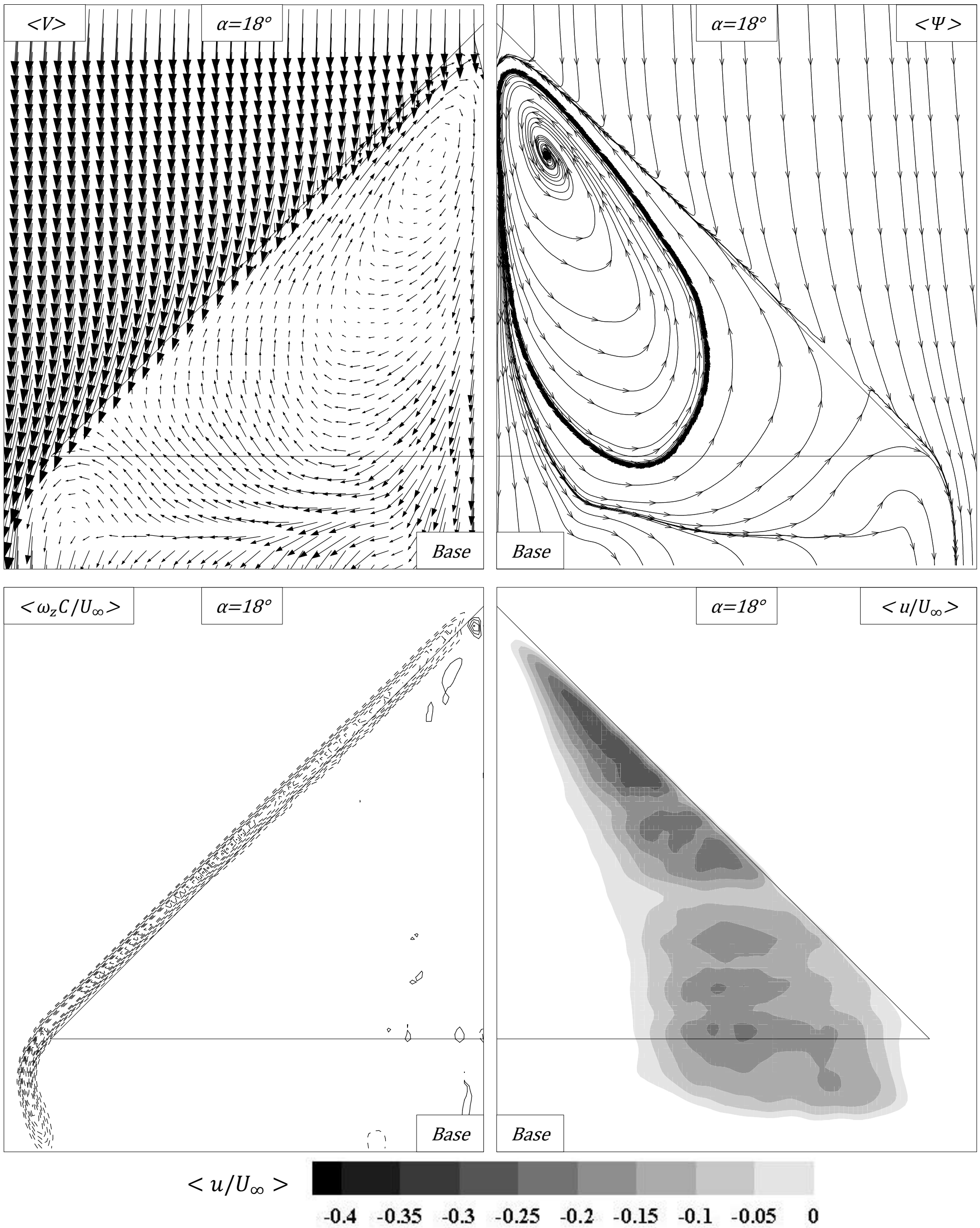

Figure 4.3: Time-averaged velocity field $\langle V \rangle$, streamline pattern $\langle \Psi \rangle$, constant contours of non-dimensional vorticity $\langle \omega_z C/U_\infty \rangle$, constant contours of non-dimensional streamwise velocity component $\langle u/U_\infty \rangle$, for the Base wing at Re = 5.0 x 10^4 and for α = 18°, $\left[|\langle \omega_z C/U_\infty \rangle| \right]_{min}$ = 6 and $\Delta\left[|\langle \omega_z C/U_\infty \rangle| \right]$ = 3, $\left[\langle u/U_\infty \rangle \right]_{min}$ = 0 and $\Delta\left[\langle u/U_\infty \rangle \right]$ = -0.05

Near-surface time-averaged streamline structures are exhibited in the Figure 4.4 for the *bor* = 0.35, 0.60, 0.85 & 1.00 wings. Except for the *bor* = 1.00 wing, the scale of the streamline focus shrinks, moreover, moves to the apex. Although, the distinction is not very obvious, the reattachment line for the *bor* = 0.85 & 1.00 wing occurs at the outboard of the symmetry line and there is a boost of the strength of reattachment. Small swirling patterns appear at the downstream of the leading edge in the streamline structure emanating from the bleed passages demonstrates the effect of the bleeding for *bor* = 0.60 & 0.85 wings, while this pattern does not exist in *bor* = 0.35 wing. This gives an idea about the amount flow passing through the bleed passages which is almost not observable over the *bor* = 0.35 wing while the flow field is enhanced compared to the Base wing. On the other hand, *bor* = 1.00 wing demonstrates a very enhanced vortex dominated and reattached flow structure. The line of reattachment is very clear and strong, and is shifted to the outboard of the symmetry line of the wing. Just after the downstream of the leading edge, streamlines separated from the reattachment line converge along a line parallel to the leading edge and it is approximately at the position of the bleed channel for the fully opened wing. Hence, comparing fully opened wing with the *bor* = 0.35 wing, considering only the traces of the effect of bleeding, influence of the bleed opening ratio draws the attention in terms of the efficiency of bleed for different *bor* values.

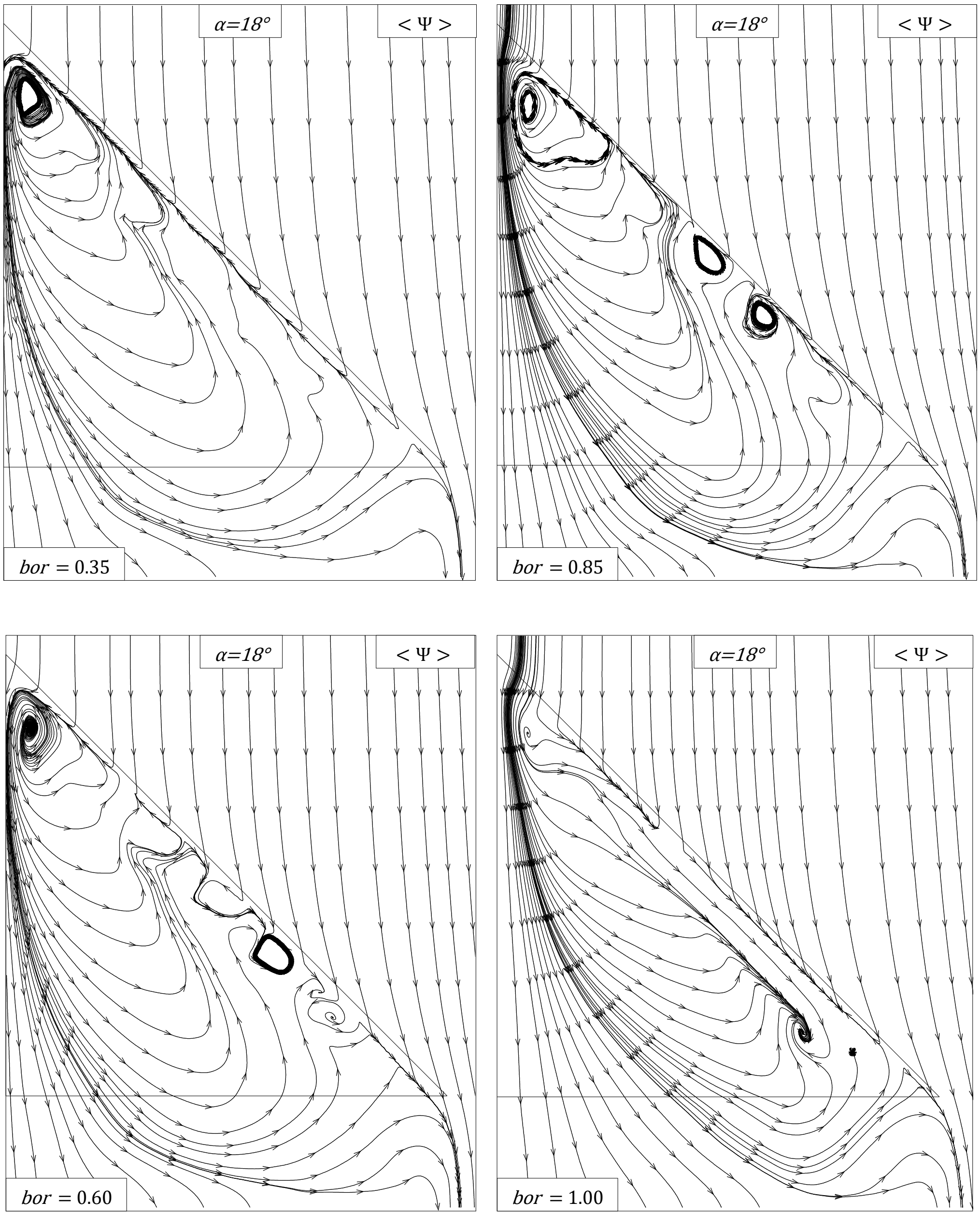

Figure 4.4: Streamline patterns $\langle\Psi\rangle$, for *bor* = 0.35, 0.60, 0.85 & 1.00 wings at Re = 5.0 x 10^4 and for α = 18°

One of very significant foot-print of three-dimensional separation over the wing is the almost stagnant velocity field in the vicinity of the wing surface. In Figure 4.3, diminish of the velocity vectors at the downstream of the leading edge is clearly shown for the Base wing, as the wing experiences the three-dimensional separation. In Figure 4.5, time-averaged velocity field is presented for four distinct *bor* wings. As the pressure measurements and the streamline contours also indicate, the *bor* = 0.35 wing does not succeed in enhancing the flow field. Velocity field of *bor* = 0.35 also results in the same scenario where velocity vectors loses its strength just after the leading edge. Likewise, velocity field of the *bor* = 0.60 wing is not very strong, although the vectors representing the swirl structure in the Base wing are disturbed. Plenty of which are still almost stagnant, yet the vectors near the symmetry line are larger in magnitude compared to the Base wing. On the other hand, for the flow field of *bor* = 0.85 wing, the area covered by the vectors with larger magnitude is dominant over approximately one-third of the half wing. The bleeding mechanism succeeded in strengthening the vectors near the symmetry line. Over the fully opened wing, as the streamline structure heralded, stagnant vector field disappeared except for the field near the trailing edge. The foot-prints of three-dimensional separation vanished, and velocity vectors, even stronger than the free stream velocity, took over the small vectors near the symmetry line. Although directly relating the outcome of this increase in the velocity magnitudes of the vectors near the symmetry line with the existence of the vortical structure might be erroneous, the improvement of flow structure compared to the Base wing is clear. The velocity vectors parallel to the leading edge also shows the effect of bleeding, which are straight and in the bleed direction. Despite that the bleed opening ratio of *bor* = 0.85 and *bor* = 1.00 is only 15 percent, flow fields differ significantly.

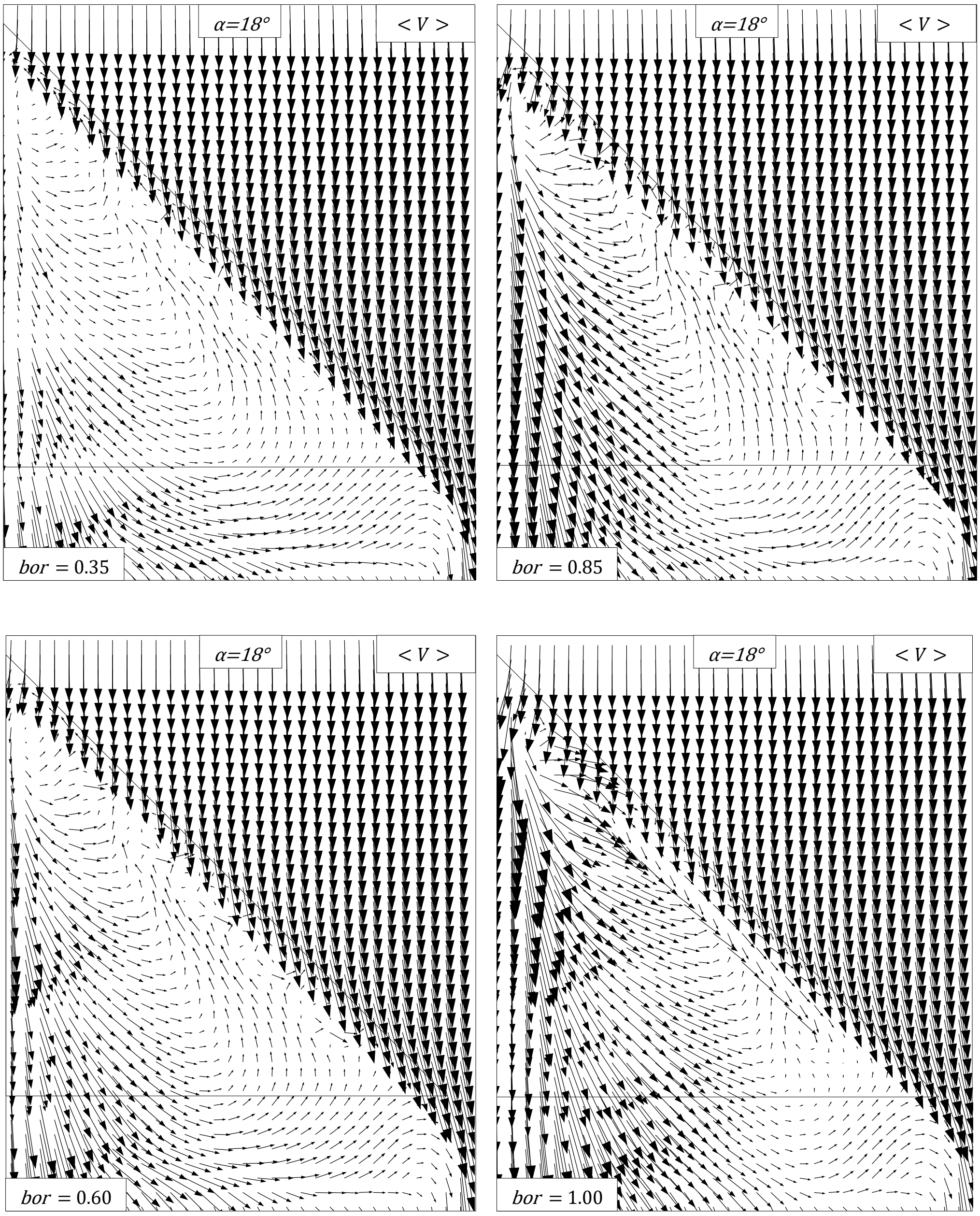

Figure 4.5: Time-averaged velocity field $\langle V \rangle$, for *bor* = 0.35, 0.60, 0.85 & 1.00 wings at Re = 5.0 x 10^4 and for α = 18°

Constant contours of non-dimensional vorticity at the surface of the plan-forms are presented in Figure 4.6. In all the wings, a field of negative vorticity contours with the dashed lines concentrated along the path of leading edge exists. The expected vorticity contour of a flow field experiencing the reattachment with a strong vortical structure is an elongated one from apex through the center of the wing. The Base wing in the pre-stall and three dimensional separation regime is lack of vorticity contour shown in Figure 4.3, except for the small vorticity structures close to the noise level. Vorticity level of *bor* = 0.35 does also not signify any improvement over the flow structure. Small scale vorticity contours appear around the region where the bleed passages are located. Concentration of the contours of *bor* = 0.60 wing in Figure 4.6 is relatively higher, although not significant. Both negative and positive small vorticity contour structures exist around the bleed passages of *bor* = 0.60 wing. On the other hand, an apparent the enhancement over the flow fields of *bor* = 0.85 & 1.00 is observable. The vorticity level is higher, especially for the *bor* = 1.00, and the vorticity contour structure elongated from the apex of the wing to the center of the plan-forms. The maximum level of vorticity concentration near the apex for *bor* = 1.00 is approximately fifty percent higher than that of *bor* = 0.85. Moreover, the location of the high vorticity concentration region is closer to the leading edge for *bor* = 1.00 wing compared to the *bor* = 0.85, which indicates the recovery of the stronger leading edge vortex over the *bor* = 1.00 plan-form. For *bor* = 0.35, 0.60 & 0.85 wings, both positive and negative circular-like vorticity contours concentrated near the leading edge are observed, while positive ones located close to the leading edge and negative ones are further, inboard to the wing center. On the other hand, this positive and negative contours exist along the same line parallel to the leading edge and the positive one closer to the apex and negative structure is closer to the trailing edge. Despite that importance of this interpretation of this positive negative vorticity structure around the leading edge is questionable, this might provide some information regarding the amount of airflow passing through the bleed passages.

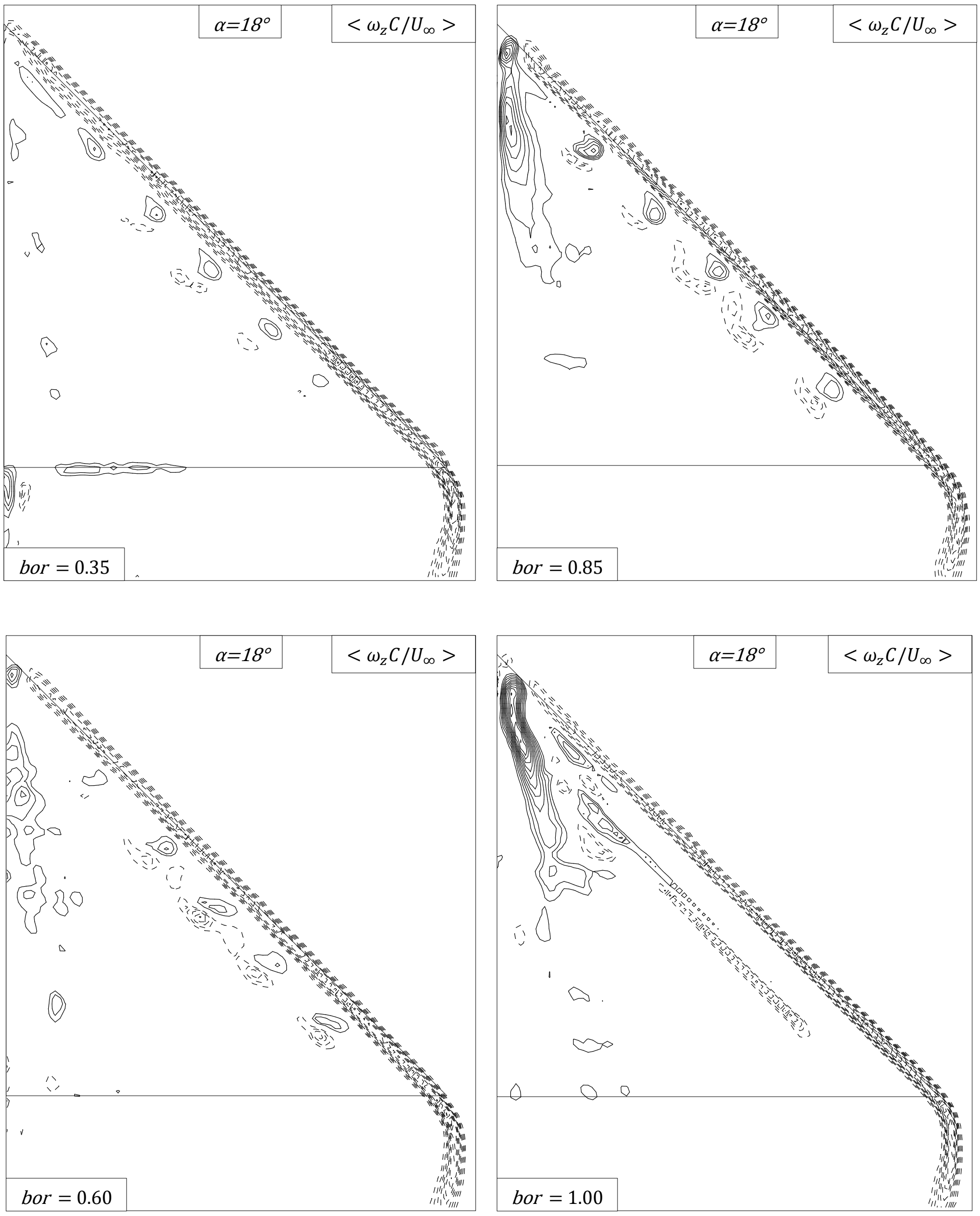

Figure 4.6: Constant contours of non-dimensional vorticity, $\langle \omega_z C/U_\infty \rangle$ for *bor* = 0.35, 0.60, 0.85 & 1.00 wings at Re = 5.0 x 10^4 and for α = 18° $\left[|\langle \omega_z C/U_\infty \rangle| \right]_{min}$ = 6 and $\Delta \left[|\langle \omega_z C/U_\infty \rangle| \right]$ = 3

In the discussion above the features of the flow structure near the suction side of the delta wings are made. Although the bleed opening ratio between the wing *bor* =

0.85 and *bor* = 1.00 is only 15 percent, the distinction between the flow feature of those are significant. In order to comment on that, in Figure 4.7, the non-dimensional streamwise velocity component $\langle u/U_\infty \rangle$ are demonstrated with the shaded areas for all wings with the bleed passages location that are extracted from the CAD software. The Base wing at α = 18° for Re = 5.0 x 10^4 experiences the three-dimensional separation and main reason for that is the adverse pressure gradient that results in the domination of the negative streamwise velocity component over the flow field presented at the bottom right of Figure 4.3. At the first sight, the negative streamwise velocity component contour structures of *bor* = 0.35, 0.60 and 0.85 appear to be quite similar and the maximum level of that are the same. Nevertheless, spatial extend of the shaded area for *bor* = 0.85 is slightly smaller than that of *bor* = 0.35 & 0.60, despite the fact that the level of maximum negative non-dimensional streamwise velocity component contours is the least for *bor* = 0.35 wing among these three wings, and this might be questionable. On the other hand, the dimensionless negative streamwise velocity component contours of *bor* = 1.00 reveal a very distinct view. Bleeding overcomes a notable portion of the area covered by the contours which supports aforementioned enhancement of the flow field of *bor* = 1.00 wing. Considering the bleed opening areas, while the lack of difference between the wings *bor* = 0.35, 0.60 and 0.85 is understandable, the significant distinction between the *bor* = 0.85 and 1.00 is remarkable. This clear distinction of the plan-forms *bor* = 0.85 & 1.00, although the bleed opening areas are quite close, might be interpreted that solid parts between the bleed passages distort air passing through the openings and reduce the effect of bleeding. Hence, rather than the bleed opening ratio, orientation of exiting flow stream from the bleed openings might be more important.

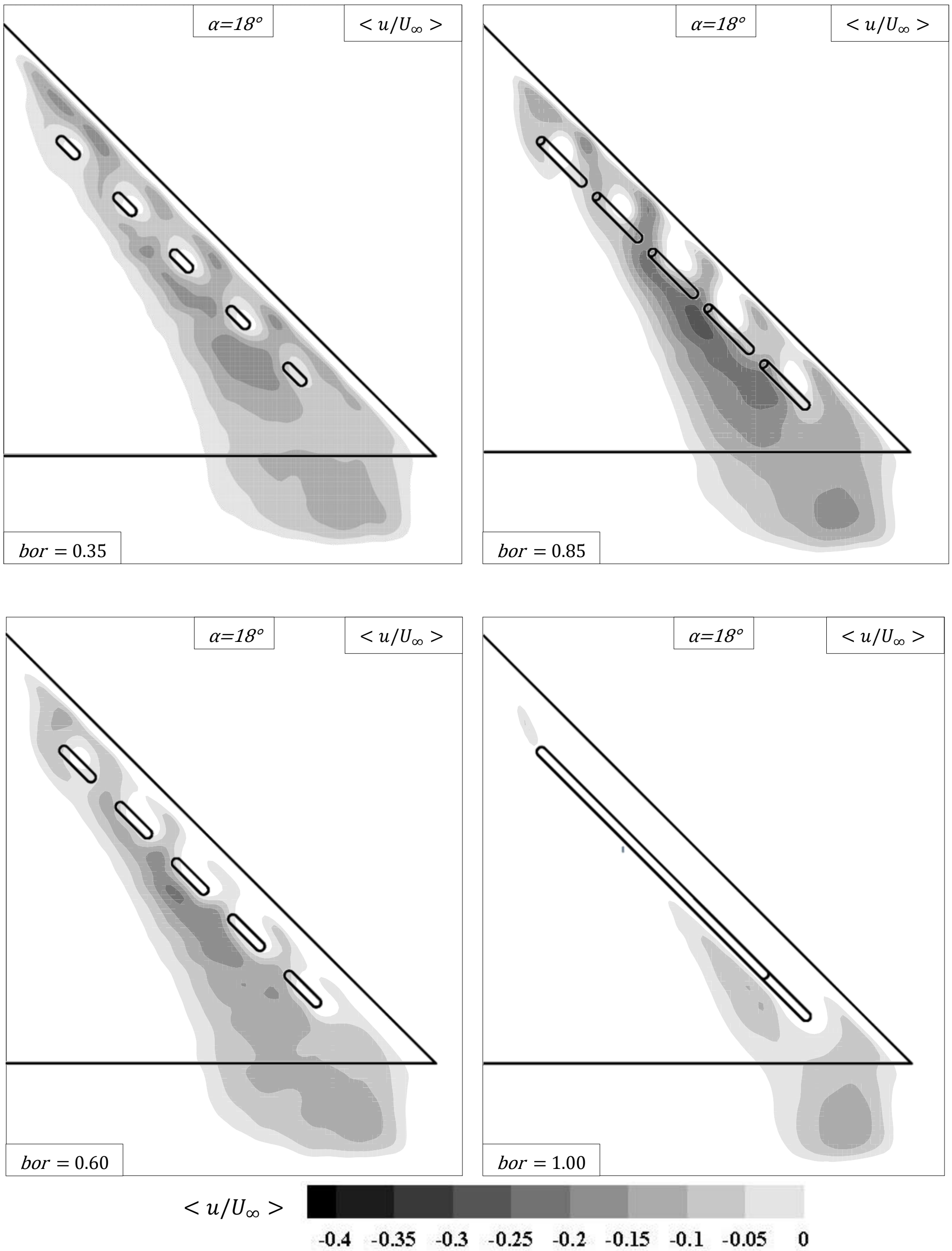

Figure 4.7: Constant contours of non-dimensional streamwise velocity component $\langle u/U_\infty \rangle$, for *bor* = 0.35, 0.60, 0.85 & 1.00 wings at Re = 5.0 x 10^4 and for α = 18°, $\left[\langle u/U_\infty \rangle\right]_{min}$ = 0 and $\Delta\left[\langle u/U_\infty \rangle\right]$ = -0.05

As it is discussed in the Chapter 2, the high velocity fluctuations are the foot-print of reattached flow to the wing surface, moreover, they exist near to the reattachment line which is observable over the streamline pattern [12]. The velocity magnitude root-mean-square contours shown on the left-hand side and streamline pattern shown at the right-hand side of the Figure 4.8 at $\alpha = 18°$ are demonstrated for *bor* = 1.00, 0.85 and Base wings in an ascending order. At this angle of attack, it was stated that the shear layer reattachment is not possible for the Base wing. Hence, the concentration of the rms contours for the Base wing is least and almost homogeneously distributed along the surface. On the other hand, rms values for *bor* = 0.85 wing near apex and the downstream of there is significantly high and the spatial extend of the relatively high rms contours follow the path of the reattachment line that is demonstrated in the adjacent streamline pattern. This is inline with the findings of Taylor and Gursul [12], although the spanwise position of the reattachment line is relatively closer to the symmetry line of the wing. The rms contours for the *bor* = 1.00 wing reveal the high concentration near the apex and around the center of the wing the concentration of the rms value reaches fifty percent higher than that of *bor* = 0.85 wing. Since the shear layer reattachment is stronger in *bor* = 1.00 wing than *bor* = 0.85 wing, the increase in the concentration of the rms contours is understandable. Nevertheless, when the adjacent streamline pattern is considered, there is a gap along the rms contours where the reattachment line is supposed to be located. It is expected to observe an rms contour concentration of which covers the area extended from apex to the wing center without the discontinuity. This might be because of the dominating flow coming through the bleed passage.

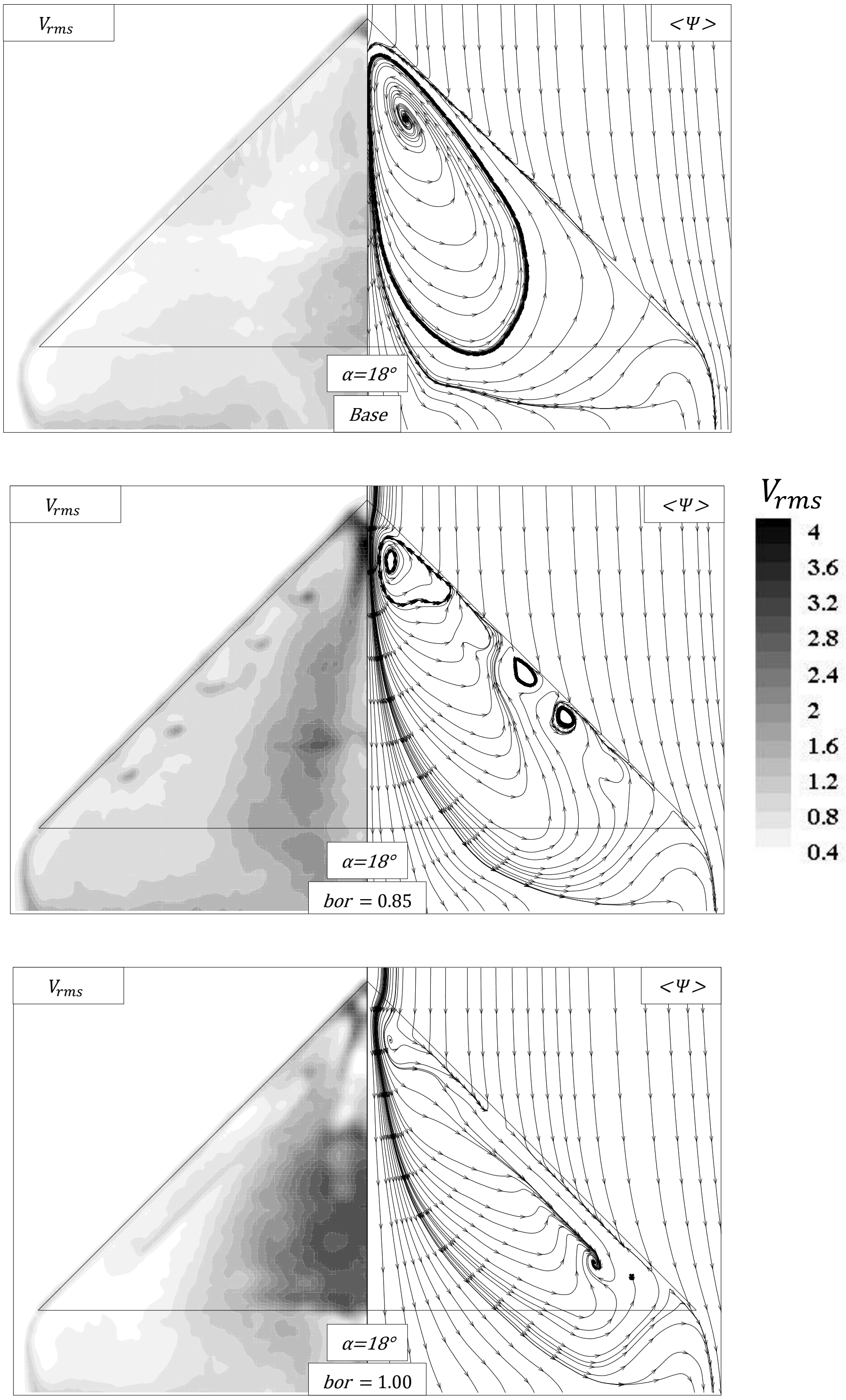

Figure 4.8: Constant contours of velocity magnitude root-mean-square (left) V_{rms}, streamline patterns (right) $\langle\Psi\rangle$, for *bor* = 0.85, 1.00 and Base wings at Re = 5.0 x 10^4 and for α = 18°, $\left[V_{rms}\right]_{min}$ = 0.4 and $\Delta\left[V_{rms}\right]$ = 0.2

Particle image velocimetry measurements were also performed for the same Reynolds number at angle of attack α = 20° for *bor* = 0.85, 1.00 and Base plan-forms. The vector field, steamline structure, non-dimensional vorticity contours and non-dimensional streamwise velocity component contours of Base, *bor* = 0.85 and *bor* = 1.00 wings are present in a descending order in Figure 4.9. The PIV results are shown as full wings by mirroring the results obtained for the half wing.

The results of the Base wing that has already experienced the three-dimensional separation at α = 18° is similar in this case as well. The velocity field is almost stagnant and decrease in that appears just after the leading edge. Structure of non-dimensional constant vorticity contours is also not visible over the Base wing. Considering the streamline structures, the large-scale focus comes with a shift in its position through the center of the plan-forms. Moreover, spatial extend of negative streamwise velocity over the Base wing almost covers the whole wing surface. The improvements observed over the *bor* = 0.85 wing seems to be lost at α = 20°. Considering the velocity field, vectors lose their strength at the downstream of the leading edge, furthermore, bleeding is not efficient enough to achieve to increase the velocity magnitude of the vectors near the symmetry line. In the incidence of angle of attack α = 18°, bleeding was capable of increasing the magnitude of the vectors near the symmetry line significantly for *bor* = 0.85 wing, whereas at α = 20° this does not happen. Streamline structure also supports the discussion regarding different scenarios for the velocity field of *bor* = 0.85 wing at different angles of attack. At α = 20°, the focus of the swirl pattern shifted to the apex and its size is smaller compared to the Base wing. Moreover, the line of reattachment is also observable, thus, bleed still enhances the flow field, although insignificant. Non-dimensional vorticity structure also lost its concentration at α = 20° for *bor* = 0.85 wing. The positive and negative small patterns still exist near the leading edge. However, foot-print of the flow reattachment that is the vorticity pattern elongated from apex to wing center does not appear except for a weak structure close to the noise level. Streamwise velocity component contours of *bor* = 0.85 might show a slight improvement over the flow field compared to Base plan-form. The size of the shaded area, which is the region where reverse flow is dominant, is smaller compared to that of the Base wing. On the other hand, the maximum value of which is higher in the *bor* = 0.85 wing. Similar contradiction between reverse flow contours of the wings *bor* = 0.35 and 0.85 is also mentioned at α = 18°. Hence, despite that the flow field of *bor* = 0.85 is slightly enhanced compared to the Base wing at α = 20°, it is not as strong as in angle of attack of 18 degree. As the pressure measurements foresee, the fully opened wing is still capable of recovering the vortical structure at α = 20°. The velocity field demonstrates that the almost stagnant field on the Base wing is replaced by the stronger vectors, relatively weaker to case at α = 18°, region near the symmetry line. The large scale focus appearing in the Base wing streamline pattern vanishes and the pattern with the reattachment line emerges. There still exists a small-scale swirl structure at the region very near to apex, yet the enhancement of the flow field with streamlines converging to the reattachment line is clear to see. Dimensionless vorticity pattern is not as strong as in case α = 18° for *bor* = 1.00, however, the concentration of the vorticity is still high around the apex. Furthermore, the pattern near the leading edge occurs due to the bleeding also keeps it position. Non-dimensional streamwise velocity component contours demonstrate the remarkable result, as in the α = 18° case, compared to the other wings, especially the Base wing where there is no flow control. Results of the *bor* = 1.00 wing for α = 20° at Re = 5.0 x 10^4 are consistent with the pressure measurement results, the flow field is enhanced, reattachment of the separated shear layer is achieved.

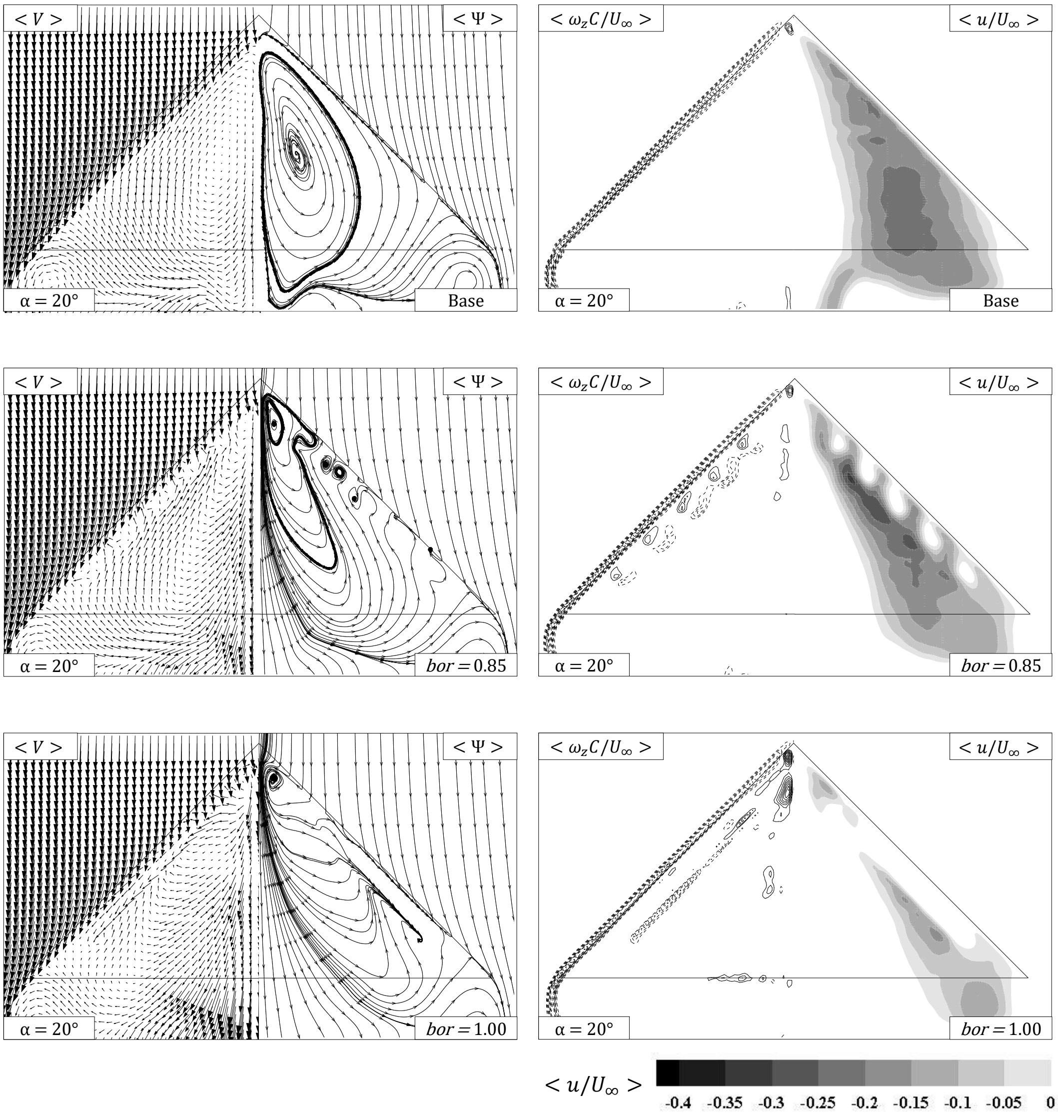

Figure 4.9: Time-averaged velocity field $\langle V \rangle$, streamline pattern $\langle \Psi \rangle$, constant contours of non-dimensional vorticity $\langle \omega_z C/U_\infty \rangle$, constant contours of non-dimensional streamwise velocity component $\langle u/U_\infty \rangle$, for *bor* = 0.85, 1.00 & Base wings at Re = 5.0 x 10^4 and for α = 20°, $\left[|\langle\langle \omega_z C/U_\infty \rangle|\right]_{min}$ = 6 and $\Delta\left[|\langle \omega_z C/U_\infty \rangle|\right]$ = 3, $\left[\langle u/U_\infty \rangle\right]_{min}$ = 0 and $\Delta\left[\langle u/U_\infty \rangle\right]$ = -0.05

In order to ensure the existence of the reattachment line and deduce its position, the contours of magnitude of rms velocity are demonstrated in Figure 4.10 for *bor* = 0.85 on the left and for *bor* = 1.00 on the right. The comparison of the level of the rms velocity contours reveals that maximum level is higher in the *bor* = 1.00 wing than *bor* = 0.85 wing. Streamline pattern of *bor* = 0.85 shown in 4.9 indicates the location of the reattachment line which is very close to the symmetry line of the wing. This is the furthest location of the shear layer reattachment line before it disappears and the wing experiences the three-dimensional separation, hence, the concentration level of the rms velocity contours are relatively less. On the other hand, the position of high level rms velocity contours and the streamline pattern with apparent shear layer reattachment line are consistent for *bor* = 1.00 wing. The high concentration appears first near the apex and elongates to the center of the wing so does the shear layer reattachment line. Thus, the reattachment exists and its location is around where the streamline structure indicates for *bor* = 1.00 wing for α = 20° at Re = 5.0 x 10^4. Further cases at higher angles of attack were not investigated with PIV since the pressure measurements also did not result in promising flow field in terms of reattachment.

The impact of bleeding with *bor* = 1.00 wing is superior to other wings and passive bleeding is efficient in the improvement of the flow field up to α = 20 degrees of angle of attack.

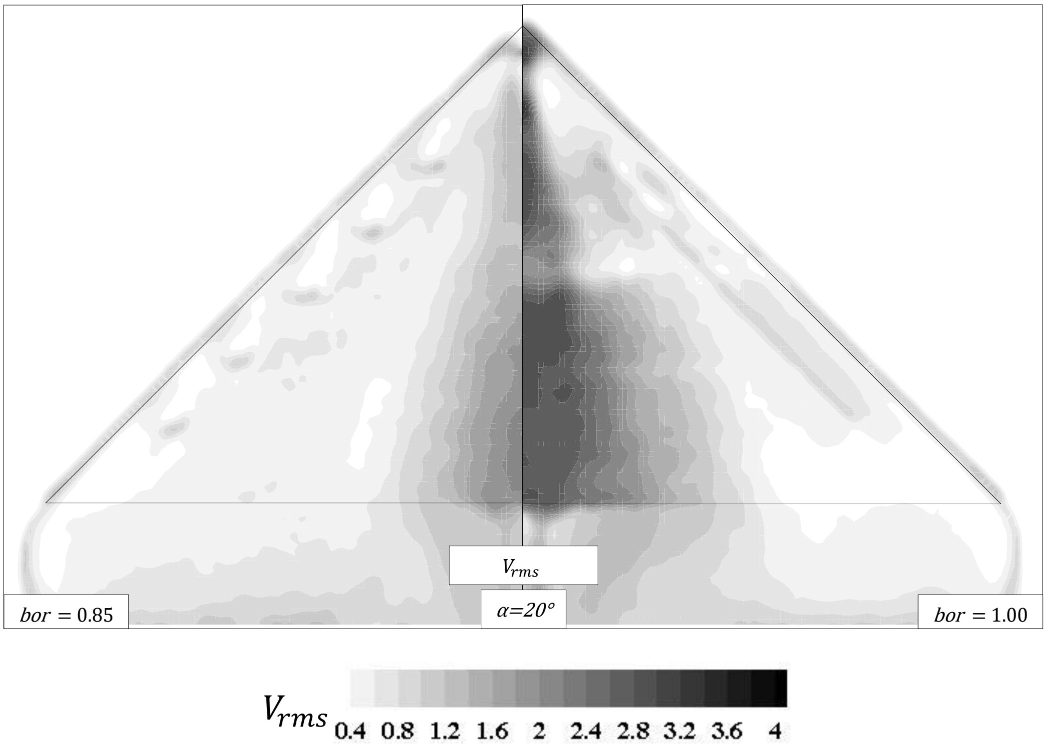

Figure 4.10: Constant contours of velocity magnitude root-mean-square V_{rms}, for *bor* = 0.85 (left) & 1.00 (right) wings at Re = 5.0 x 10^4 and for α = 20°, $\left[V_{rms}\right]_{min}$ = 0.4 and $\Delta\left[V_{rms}\right]$ = 0.2

4.3 Results of Force Measurements

The outcomes of passive bleeding in terms of the stability of the flow field, the shear layer reattachment and the regeneration of vortical structure are significantly promising as mentioned above. Moreover, the distinction between the wings is clear enough to discuss the bleed opening ratio influence. Yet, there always exist a certain ambiguity regarding the aerodynamic forces over the wings with passive bleeding since the method inherently diminishes the pressure difference between the wing surfaces which might cause the decrease in the lift force, although regeneration of leading edge vortex is expected to augment the lift force.

Non-dimensional lift C_L, and drag coefficient C_D, as well as the lift-to-drag ratio, C_L/C_D are presented in Figure 4.11 for Reynolds number Re = 1 x 10^5 for angles of attack in the span of $0° \geq \alpha \geq 36°$. Since the stall is expected to occur around $10° \geq \alpha \geq 25°$, the increment of the angle for data acquisition is different. For angle of attack of $0° \geq \alpha \geq 9°$ and $27° \geq \alpha \geq 36°$ the increment is 1.8° while for $9.9° \geq \alpha \geq 25.2°$ the increment of α is 0.9° which is more precise compared to increment of 1.8°. Measurements were also performed for the Reynolds number Re = 5.0 x 10^4, nevertheless, wings experience the force in the lower limitations of the utilized force measurement sensor. Hence, the results at Re = 1 x 10^5 have less uncertainty values and curves are smoother. The graph containing the measurements at Re = 5.0 x 10^4 is in Appendix A. Furthermore, the data used in the charts are in the table attached to Appendix B.

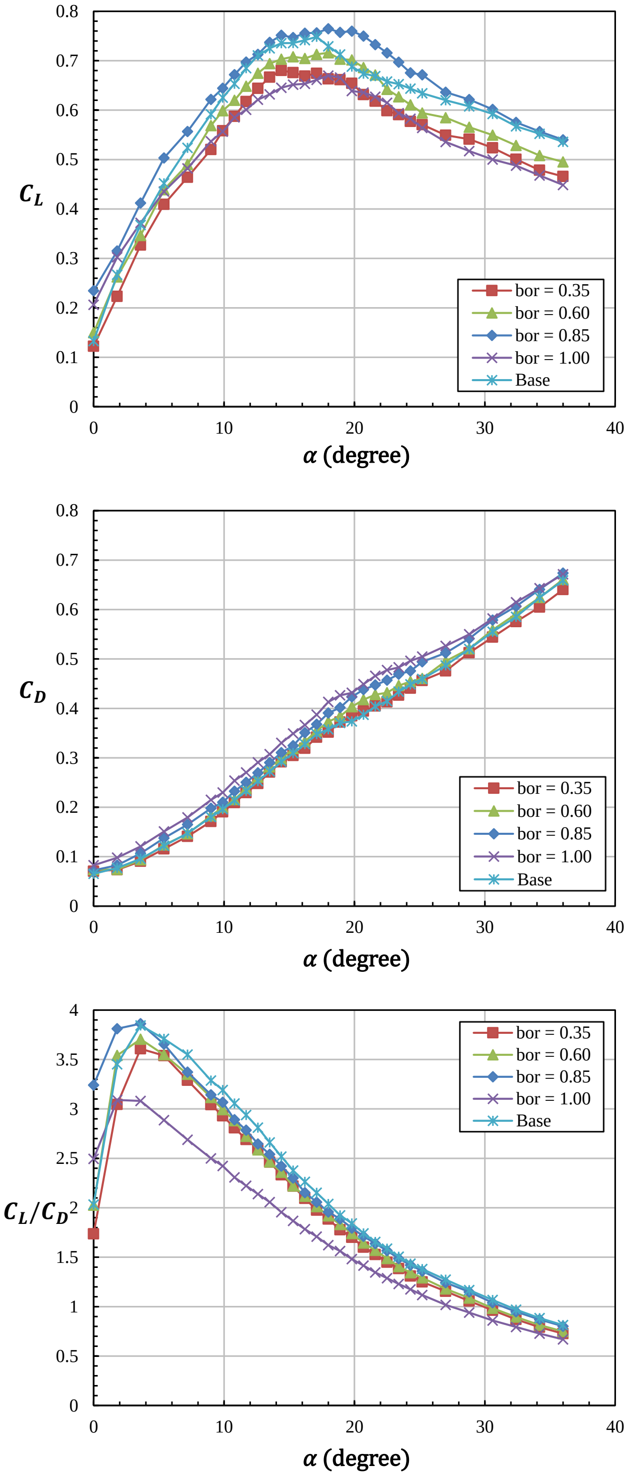

Figure 4.11: Non-dimensional lift coefficient C_L, drag coefficient C_D and lift-to-drag ratio C_L/C_D from top to bottom respectively, for *bor* = 0.35, 0.60, 0.85, 1.00 & Base wings at Re = 1 x 10^5 for $0° \geq \alpha \geq 36°$

The first chart on top at Figure 4.11 demonstrates the dimensionless lift coefficient, C_L, versus angles of attack, α, for *bor* = 0.35, 0.60, 0.85, 1.00 and Base plan-forms. Base wing shown with the light blue line have a trend starting just above C_L = 0.1 and experienced stall approximately at α = 17 degrees. The maximum lift coefficient over the Base wing is around 0.75 after which the expected decrease of the trend of C_L is observed. The second wing *bor* = 0.35, the line of which is illustrated with the red line, also have a lift coefficient slightly larger than 0.1 at α = 0 degree. This plan-form experiences the stall at around α = 15 degrees. The general trend of the C_L of *bor* = 0.35 wing is just below the C_L graph of Base wing, which is expected due to the aforementioned flow field. The bleed mechanism decreases the pressure difference between the suction and pressure sides of the *bor* = 0.35 wing, in addition, the flow structure of the wing is not improved. Hence, C_L measurements matches with the previous results. The third wing *bor* = 0.60 is illustrated with the green line and the similar C_L value shows up at angle of attack α = 0°. The lift coefficient values are always higher than the *bor* = 0.35 wing, furthermore, the stall is observed at angle of attack around α = 18 degrees. Although the flow field over this wing is not significantly enhanced compared to the Base wing, the stall angle seems to retard although the lift force over the wing is less than the Base wing in general. The superior results in terms of lift coefficient appear in the *bor* = 0.85 wing which is illustrated with the dark blue line in the C_L chart. The wing posses the C_L value over the 0.2 at angle of attack of 0 degree. Furthermore, the lift force over the wing is highest among others including the Base wing, although the C_L values of those coincide around the angles of attack between approximately 10° to 17°. The *bor* = 0.85 wing experiences the stall at angle of attack slightly further than α = 20° and after that the trend of the C_L line is still above others. This points out the achievement of the delay of the stall angle. The last wing *bor* = 1.00 has a similar C_L value at zero attack angle, just above 0.2. Although at low angles of attack, the C_L curve of *bor* = 1.00 wing is above others, after 10 degrees of angle of attack, this wing starts experience the least lift force compared to other, which is expected due to the bleeding. The stall angle for this wing appears as around α = 19 degrees. Stall angle is delayed compared to the Base wing, albeit that the difference is only around 2 degrees, furthermore, the C_L is almost doubled compared to the Base wing at zero degree of angle of attack which is a favorable feature in the design of an aircraft. Among all wings, *bor* = 0.85

draws the attention due to its superiority in terms of C_L. It has the highest values of lift force and experiences the stall at latest attack angle.

The non-dimensional drag coefficients, C_D, are demonstrated in the middle graph in Figure 4.11. While the drawback of the passive bleeding is the reduction of the pressure difference between the wing surfaces, bleeding is expected to the decrease the drag since the air freely flows through the bleed passages. Nevertheless, this may not be the outcome of the measurements. The trends of the C_D curves for all wings are almost the same. The least value is just below 0.1 and there is a small hump just before α = 20°. The curves are illustrated with the same colors as in the lift charts. Values of C_D for *bor* = 0.35, 0.60 and Base wings are almost matching. Yet, as the bleed opening enlarges the C_D value appears to increase as well. The C_D curve of *bor* = 0.85 is above the other three wings and on top of all, the line of *bor* = 1.00 is placed. The starting and the ending points of the curves are very similar for all wings yet, in a broad range of angles of attack, the trend of the C_D curve of *bor* = 0.85 and 1.00 is above others.

The lift-to-drag ratio, C_L/C_D, is also an important parameter to comment about the effectiveness of an aircraft. The bottom chart in Figure 4.11 shows the results obtained for lift-to-drag ratio. In general, all the curves reach a peak value followed by a sharp decrease at low angles of attack and converge to a value of approximately 0.75 at angle of attack α = 36°. The C_L/C_D value for the Base wing at α = 0° is approximately 2. Then the curve reaches its peak value of C_L/C_D = 3.8 at 3.6 degree. The second wing *bor* = 0.35 has C_L/C_D value of 1.75 at zero attack angle and its peak value is around 3.6 at 3.6 degree. The similar trend is observed for the *bor* = 0.60 wing although its C_L/C_D value is 2 at zero attack angle and the value is just above 3.6 at angle of attack of 3.6 degrees. The C_L/C_D curve of *bor* = 0.85 has highest values among others at low angles of attack, which are 3.25 at α = 0 degree and 3.9 at α = 3.6 degrees. Lastly, as it is predictable considering the C_L and C_D charts, the least value of the peak of C_L/C_D is observed in the curve of *bor* = 1.00 wing, which is around 3.1 at both α = 1.8° & 3.6°. The value of C_L/C_D for this wing is also around 2.5 at α = 0 degree. Up to the angle of attack α = 3.6 degrees, the C_L/C_D values are higher for the *bor* = 0.85 wing, nevertheless, for the rest of the attack angles Base wing demonstrates the superior values. The C_L/C_D curve of *bor*

= 1.00 is below of others and the values of which are significantly lower than the rest at all angles of attack, although they converge to a same value. It should be noted that at α = 0°, both *bor* = 0.85 and 1.00 wings have C_L/C_D values higher than Base wing. Despite that the C_L/C_D performance of *bor* = 1.00 wing is inferior in an large range of angle of attack, for an aircraft design to have high C_L/C_D value at the angles of attack corresponding to the take-off incidences is an advantage.

CHAPTER 5

CONCLUSION

Present study aims to comprehend the effect of bleed opening ratio for the 45 degree swept delta wings with passive bleed control at the extremities of the flight conditions. In order to achieve this, wings with four different bleed opening ratio, *bor* = 0.35, 0.60, 0.85 and 1.00 are compared with the Base wing over which passive bleeding mechanism is not applied. The measurements were performed in mainly at two Reynolds number Re = 5.0 x 10^4 and 1 x 10^5 for attack angles $0^\circ \geq \alpha \geq 36^\circ$ employing particle image velocimetry, force measurement and surface pressure measurement. Since the study is devoted to compare the bleed opening ratio, the comparison of the *bor* wing is made at the cases where the Base wing is already pre-stall/stall regime and experiences the three-dimensional separation.

According to the results presented in the previous chapter, following conclusions may be deduced:

- At all angles of attack where the Base wing is in pre-stall/stall regime or experiences the three-dimensional separation, *bor* = 0.35 wing also does not perform any improvement in terms of the enhancement of the flow field. Furthermore, considering the lift performance and lift-to-drag ratio over the entire angles of attack studied in the measurements, *bor* = 0.35 wing demonstrated worse results compared to the Base wing, while drag coefficient are almost identical for both wings.

- The plan-form with *bor* = 0.60 demonstrated promising performance in the reattachment of the flow field at Reynolds Number Re = 1 x 10^5, up to the angle of attack $\alpha = 18^\circ$, considering only the pressure measurement results.

Moreover, although the sufficiency is arguable, the enhancement over the flow field at the suction side of the *bor* = 0.60 wing is observed in the near-surface PIV measurements at α = 18 degree. The expected decrease in lift force over the wing is also present as the force measurements point out.

- Considering the effectiveness in terms of flow reattachment and vortex recovery, *bor* = 0.85 wing appears to be the second most effective wing. Pressure measurements demonstrate that the vortex recovery is achievable up to angle of attack α = 18 degree, moreover, the near-surface PIV findings support the amelioration of the flow field due to the existing foot-print of shear layer reattachment to the wing surface. Furthermore, the superiority of the wing in the lift force measurements over all other bleed controlled wings and Base wing draws the attention, especially in the lift and lift-to-drag ratio findings at zero degree of angle of attack.

- Fully opened wing with bleed opening ratio *bor* = 1.00 might be said to be the most efficient according to the results obtained considering the flow fields. The surface pressure measurements show promising results in terms of recovery of the vortical structure up to the angle of attack of 20 degrees. Moreover, reattachment of the separated shear layer and the recovery of leading edge vortex are clearly observed up to α = 20°. Fully opened wing also retards to stall angle and increased the C_L/C_D ratio value at zero degree of angle of attack, which is an important feature for an aircraft at the take-off incidence, compared to the Base wing, albeit that the lift coefficients are significantly less than that of the Base plan-form.

Remarks:

- As the bleed opening ratio increases, the flow field over the non-slender delta wings seems to enhance according to the present study. Particularly for the fully opened wing, the amelioration of the flow field may be said to be significant at angles of attacks up to α = 20°.

- Fully opened wing is capable of reattaching the shear layer separation and recovering the vortical structure up to 20 degrees of angles of attack. Nevertheless, the force measurements showed that the lift force over the fully opened wing is significantly less than Base wing, which is expected due to the presence of bleeding, yet, the stall is delayed on fully opened wing relative to the Base wing. This might be one of the remarkable conclusion of the present study. It is, however, hard to reason, since the lift contribution of the vortical structure to the non-slender delta wings is relatively low. Moreover, the second most efficient wing with bleed opening ratio *bor* = 0.85 resulted in ambiguous findings such that the near-surface PIV showed relatively less recovery in the vortical structure and reattachment is not perfectly achieved at α = 20 degree. Nonetheless, over the entire span of angles of attack in force measurements, superiority of the *bor* = 0.85 wing was clear in terms of lift coefficient. The lift is higher than the Base wing and *bor* = 1.00 wing, furthermore, the wing experience the stall at the latest angle of attack among others.

- It is also relatively difficult to deduce a clear result from the drag coefficient graph. The bleed mechanism is expected to decrease the drag force existing over the wing, however, the force measurements reveal that trend of the drag coefficient curve, C_D, of fully opened wing is above among others over the entire range of angles of attack, and that of *bor* = 0.85 shows up just below the curve of fully opened wing. Although the C_D of other bleed wings are approximately the same, it is hard to draw a reasonable conclusion from these findings.

- As viscous flow theory states, the adverse pressure gradient causes flow to separate. One of the very first technique to overcome this issue is to introduce momentum against the adverse pressure gradient. Basically, the bleeding also aims that, moreover, findings supported this theory as the bleed opening enlarges the momentum transfer increases, hence, enhancement in the flow field with strong vortices is observed. Fully opened wing exhibited a superior performance among others in terms of flow reattachment and recovery of the vortex and the *bor* = 0.85 wing shows up as the second most effective. Despite that this is expected, the difference between the bleeding surface area of these two wings is only 15 percent, yet, the flow structure and lift coefficients demonstrates significant divergence. The issue might be because of two reasons; either bleed effectiveness is really sensitive to the bleed opening ratio for over certain *bor* values or the solid parts dividing the bleed channels distort the flow exiting from the passages in an inefficient way.

Passive bleed is proved to be an efficient flow control mechanism in a certain range of angle of attack [16, 17]. In this study, the motivation was to exhibit whether the bleeding is sufficient at high angles of attack by changing the bleed opening ratio. It might be concluded that bleed opening ratio is an important parameter over the efficiency of passive bleeding, and active bleed mechanisms with a variable bleed openings could be implemented over delta wings in order to satisfy the flight stability at the extremities.

5.1 Future Extensions to the Study

This present study employs an experimental approach to comprehend the possible effects of the bleed opening ratio to the flow field and among limitless bleed orientations a proved one in literature is studied [16]. In order to explore further, the extension to the study might focus on the elimination of negative streamwise velocity component. When the negative streamwise velocity component contours are observed, it could be deduced that elimination of the reverse flow eases the recovery of the leading edge vortex. Hence, configuration and the orientation of the bleed holes might be set such that the air passing throughout the bleed passages goes to the center of the region where the negative streamwise velocity is dominant. To illustrate, bleed holes might be located where the maximum values in the streamwise velocity component highest for the Base wing shown in Figure 4.3.

REFERENCES

[1] M. Meyer and C. Breitsamter, “Aerodynamic characteristics of the blended wing body acfa2020,” in *New Results in Numerical and Experimental Fluid Mechanics VIII*, pp. 51–58, Springer, 2013.

[2] R. T. Jones, “The minimum drag of thin wings in frictionless flow,” *Journal of the Aeronautical Sciences*, vol. 18, no. 2, pp. 75–81, 1951.

[3] R. Denning, J. Allen, and F. Armstrong, “Future large aircraft design—the delta with suction,” *The Aeronautical Journal*, vol. 101, no. 1005, pp. 187–198, 1997.

[4] R. H. Liebeck, “Design of the blended wing body subsonic transport,” *Journal of aircraft*, vol. 41, no. 1, pp. 10–25, 2004.

[5] I. Gursul, Z. Wang, and E. Vardaki, “Review of flow control mechanisms of leading-edge vortices,” *Progress in Aerospace Sciences*, vol. 43, no. 7-8, pp. 246–270, 2007.

[6] I. Gursul, “Vortex flows on uavs: Issues and challenges,” *The Aeronautical Journal*, vol. 108, no. 1090, pp. 597–610, 2004.

[7] P. Earnshaw and J. Lawford, *Low-speed wind-tunnel experiments on a series of sharp-edged delta wings*. HM Stationery Office London, 1966.

[8] I. Gursul, R. Gordnier, and M. Visbal, “Unsteady aerodynamics of nonslender delta wings,” *Progress in Aerospace Sciences*, vol. 41, no. 7, pp. 515–557, 2005.

[9] M. Visbal and R. Gordnier, “On the structure of the shear layer emanating from a swept leading edge at angle of attack,” in *33rd AIAA Fluid Dynamics Conference and Exhibit*, p. 4016, 2003.

[10] I. Gursul, “Review of unsteady vortex flows over slender delta wings,” *Journal of Aircraft*, vol. 42, no. 2, pp. 299–319, 2005.

[11] C. Breitsamter, "Unsteady flow phenomena associated with leading-edge vortices," *Progress in Aerospace Sciences*, vol. 44, no. 1, pp. 48–65, 2008.

[12] G. Taylor and I. Gursul, "Unsteady vortex flows and buffeting of a low sweep delta wing," in *42nd AIAA Aerospace Sciences Meeting and Exhibit*, p. 1066, 2003.

[13] S. Z. Pirzadeh, "Vortical flow prediction using an adaptive unstructured grid method," tech. rep., NATIONAL AERONAUTICS AND SPACE ADMINISTRATION HAMPTON VA LANGLEY RESEARCH CENTER, 2003.

[14] B. Gülsaçan, G. Şencan, and M. M. Yavuz, "Effect of thickness-to-chord ratio on flow structure of a low swept delta wing," *AIAA Journal*, vol. 56, no. 12, pp. 4657–4668, 2018.

[15] J. Kearney and A. Glezer, "Aerodynamic control using distributed bleed," in *6th AIAA Flow Control Conference*, p. 3246, 2012.

[16] A. Çelik, C. Çetin, and M. M. Yavuz, "Effect of passive bleeding on flow structure over a nonslender delta wing," *AIAA Journal*, pp. 2555–2565, 2017.

[17] B. Karagoz, "Control of flow structure on 45 degree swept angle delta wing using passive bleeding," Master's thesis, Middle East Technical University, Ankara, Turkey, 2017.

[18] I. Gursul and W. Xie, "Origin of vortex wandering over delta wings," *Journal of Aircraft*, vol. 37, no. 2, pp. 348–350, 2000.

[19] R. C. Nelson and A. Pelletier, "The unsteady aerodynamics of slender wings and aircraft undergoing large amplitude maneuvers," *Progress in Aerospace Sciences*, vol. 39, no. 2-3, pp. 185–248, 2003.

[20] E. C. Polhamus, "Predictions of vortex-lift characteristics by a leading-edge suctionanalogy," *Journal of aircraft*, vol. 8, no. 4, pp. 193–199, 1971.

[21] I. Gursul, G. Taylor, and C. Wooding, "Vortex flows over fixed-wing micro air vehicles," in *40th AIAA Aerospace Sciences Meeting & Exhibit*, p. 698, 2002.

[22] M. V. Ol and M. Gharib, "Leading-edge vortex structure of nonslender delta wings at low reynolds number," *AIAA journal*, vol. 41, no. 1, pp. 16–26, 2003.

[23] R. E. Gordnier and M. R. Visbal, “Compact difference scheme applied to simulation of low-sweep delta wing flow.,” *AIAA journal*, vol. 43, no. 8, pp. 1744–1752, 2005.

[24] M. S. Ghazijahani and M. M. Yavuz, “Effect of thickness-to-chord ratio on aerodynamics of non-slender delta wing,” *Aerospace Science and Technology*, 2019.

[25] J. M. Delery, “Aspects of vortex breakdown,” *Progress in Aerospace Sciences*, vol. 30, no. 1, pp. 1–59, 1994.

[26] O. Lucca-Negro and T. O’doherty, “Vortex breakdown: a review,” *Progress in energy and combustion science*, vol. 27, no. 4, pp. 431–481, 2001.

[27] F. Payne, T. Ng, R. Nelson, and L. Schiff, “Visualization and wake surveys of vortical flow over a delta wing,” *AIAA journal*, vol. 26, no. 2, pp. 137–143, 1988.

[28] M. Zharfa, I. Ozturk, and M. M. Yavuz, “Flow structure on nonslender delta wing: Reynolds number dependence and flow control,” *AIAA Journal*, vol. 54, no. 3, pp. 880–897, 2016.

[29] A. Honkan and J. Andreopoulos, “Instantaneous three-dimensional vorticity measurements in vortical flow over a delta wing,” *AIAA journal*, vol. 35, no. 10, pp. 1612–1620, 1997.

[30] G. S. Taylor and I. Gursul, “Buffeting flows over a low-sweep delta wing,” *AIAA journal*, vol. 42, no. 9, pp. 1737–1745, 2004.

[31] M. M. Yavuz and D. Rockwell, “Identification and control of three-dimensional separation on low swept delta wing,” *AIAA journal*, vol. 44, no. 11, pp. 2805–2811, 2006.

[32] M. Gad-el Hak, “Flow control: The future,” *Journal of Aircraft*, vol. 38, no. 3, pp. 402–418, 2001.

[33] G. Taylor, Z. Wang, E. Vardaki, and I. Gursul, “Lift enhancement over flexible nonslender delta wings,” *AIAA journal*, vol. 45, no. 12, pp. 2979–2993, 2007.

[34] D. Greenwell, “Gurney flaps on slender and nonslender delta wings,” *Journal of Aircraft*, vol. 47, no. 2, pp. 675–681, 2010.

[35] N. Verhaagen, "Leading-edge radius effects on aerodynamic characteristics of 50-degree delta wings," *Journal of Aircraft*, vol. 49, no. 2, pp. 521–531, 2012.

[36] B. Yaniktepe and D. Rockwell, "Flow structure on diamond and lambda planforms: Trailing-edge region," *AIAA journal*, vol. 43, no. 7, pp. 1490–1500, 2005.

[37] J. E. Lamar and J. F. Campbell, "Vortex flaps-advanced control devices for supercruise fighters," 1984.

[38] R. Bradley and W. Wray, "A conceptual study of leading-edge-vortex enhancement by blowing," *Journal of aircraft*, vol. 11, no. 1, pp. 33–38, 1974.

[39] N. Wood, L. Roberts, and Z. Celik, "Control of asymmetric vortical flows over delta wings at high anglesof attack," *Journal of Aircraft*, vol. 27, no. 5, pp. 429–435, 1990.

[40] D. Greenwell and N. Wood, "Roll moment characteristics of asymmetric tangential leading-edge blowing on a delta wing," *Journal of aircraft*, vol. 31, no. 1, pp. 161–168, 1994.

[41] J. S. Hong, Z. Z. Celik, and L. Roberts, "Effects of leading-edge lateral blowing on delta wing aerodynamics," *AIAA journal*, vol. 34, no. 12, pp. 2471–2478, 1996.

[42] W. Gu, O. Robinson, and D. Rockwell, "Control of vortices on a delta wing by leading-edge injection," *AIAA journal*, vol. 31, no. 7, pp. 1177–1186, 1993.

[43] A. Kölzsch and C. Breitsamter, "Vortex-flow manipulation on a generic delta-wing configuration," *Journal of Aircraft*, vol. 51, no. 5, pp. 1380–1390, 2014.

[44] N. M. Williams, Z. Wang, and I. Gursul, "Active flow control on a nonslender delta wing," *Journal of Aircraft*, vol. 45, no. 6, pp. 2100–2110, 2008.

[45] C. Çetin, A. Çelik, and M. M. Yavuz, "Control of flow structure over a nonslender delta wing using periodic blowing," *AIAA Journal*, pp. 90–99, 2017.

[46] P. V. Vorobieff and D. O. Rockwell, "Vortex breakdown on pitching delta wing: control by intermittent trailing-edge blowing," *AIAA journal*, vol. 36, no. 4, pp. 585–589, 1998.

[47] M. M. Yavuz and D. Rockwell, “Control of flow structure on delta wing with steady trailing-edge blow,” *AIAA journal*, vol. 44, no. 3, pp. 493–501, 2006.

[48] P. Jiang, Z. Wang, and I. Gursul, “Effects of unsteady trailing-edge blowing on delta wing aerodynamics,” *Journal of Aircraft*, vol. 47, no. 2, pp. 591–602, 2010.

[49] H. Johari, D. Olinger, and K. Fitzpatrick, “Delta wing vortex control via recessed angled spanwise blowing,” *Journal of aircraft*, vol. 32, no. 4, pp. 804–810, 1995.

[50] A. Sreenatha and T. Ong, “Wing rock suppression using recessed angle spanwise blowing,” *Journal of aircraft*, vol. 39, no. 5, pp. 900–903, 2002.

[51] H. Johari and J. Moreira, “Delta wing vortex manipulation using pulsed and steady blowing during ramp-pitching,” *Journal of aircraft*, vol. 33, no. 2, pp. 304–310, 1996.

[52] C.-H. Kuo and N.-Y. Lu, “Unsteady vortex structure over delta-wing subject to transient along-core blowing,” *AIAA journal*, vol. 36, no. 9, pp. 1658–1664, 1998.

[53] H. Helin and C. Watry, “Effects of trailing-edge jet entrainment on delta wing vortices,” *AIAA journal*, vol. 32, no. 4, pp. 802–804, 1994.

[54] Z.-J. Wang, P. Jiang, and I. Gursul, “Effect of thrust-vectoring jets on delta wing aerodynamics,” *Journal of Aircraft*, vol. 44, no. 6, pp. 1877–1888, 2007.

[55] K. Parmenter and D. Rockwell, “Transient response of leading-edge vortices to localized suction,” *AIAA journal*, vol. 28, no. 6, pp. 1131–1133, 1990.

[56] S. McCormick and I. Gursul, “Effect of shear-layer control on leading-edge vortices,” *Journal of Aircraft*, vol. 33, no. 6, pp. 1087–1093, 1996.

[57] B. Badran, S. McCormick, and I. Gursul, “Control of leading-edge vortices with suction,” *Journal of aircraft*, vol. 35, no. 1, pp. 163–165, 1998.

[58] Q. Deng and I. Gursul, “Vortex breakdown over a delta wing with oscillating leading edge flaps,” *Experiments in Fluids*, vol. 23, no. 4, pp. 347–352, 1997.

[59] J. Wang, Y. Li, and K.-S. Choi, "Gurney flap—lift enhancement, mechanisms and applications," *Progress in Aerospace sciences*, vol. 44, no. 1, pp. 22–47, 2008.

[60] I. Gursul and G. Batta, "Active control of vortex breakdown over a delta wing," *AIAA journal*, vol. 33, no. 9, pp. 1743–1745, 1995.

[61] Y. Liu, L. Zuo, and J. Wang, "Effects of flexibility on aerodynamic performance of delta wings with different sweep angles," *Science China Physics, Mechanics and Astronomy*, vol. 53, no. 5, pp. 915–922, 2010.

[62] J. Wang and S. Lu, "Effects of leading-edge bevel angle on the aerodynamic forces of a non-slender 50° delta wing," *The Aeronautical Journal*, vol. 109, no. 1098, pp. 403–407, 2005.

[63] A. Çelik and M. M. Yavuz, "Effect of edge modifications on flow structure of low swept delta wing," *AIAA Journal*, no. null, pp. 1789–1797, 2016.

[64] H. Chen and J.-J. Wang, "Vortex structures for flow over a delta wing with sinusoidal leading edge," *Experiments in fluids*, vol. 55, no. 6, p. 1761, 2014.

[65] T. Goruney and D. Rockwell, "Flow past a delta wing with a sinusoidal leading edge: near-surface topology and flow structure," *Experiments in fluids*, vol. 47, no. 2, pp. 321–331, 2009.

[66] H. Chen, C. Pan, and J. Wang, "Effects of sinusoidal leading edge on delta wing performance and mechanism," *Science China Technological Sciences*, vol. 56, no. 3, pp. 772–779, 2013.

[67] K. Sheppard and D. Rival, "On the high-lift characteristics of a bio-inspired, slotted delta wing," *Bioinspiration & biomimetics*, vol. 13, no. 3, p. 036008, 2018.

[68] G. Lachmann, "Results of experiments with slotted wings," 1924.

[69] C. Hunter, S. Viken, R. Wood, and S. Bauer, "Advanced aerodynamic design of passive porosity control effectors," in *39th Aerospace Sciences Meeting and Exhibit*, p. 249, 2001.

[70] S. X. Bauer and M. J. Hemsch, “Alleviation of side force on tangent-ogive forebodies using passive porosity,” *Journal of Aircraft*, vol. 31, no. 2, pp. 354–361, 1994.

[71] P. W. Carpenter and L. J. Porter, “Effects of passive porous walls on boundary-layer instability,” *AIAA journal*, vol. 39, no. 4, pp. 597–604, 2001.

[72] M. Zharfa, “Control of flow structure on low swept delta wing with steady leading edge blowing,” Master’s thesis, Middle East Technical University, Ankara, Turkey, 2015.

[73] C. Tropea and A. L. Yarin, *Springer handbook of experimental fluid mechanics*, vol. 1. Springer Science & Business Media, 2007.

[74] S. Kline and F. McClintock, “Describing uncertainties in single-sample experiments,,” *Mech Eng., 75, pp. 3*, vol. 8, 1953.

[75] J. J. Charonko and P. P. Vlachos, “Estimation of uncertainty bounds for individual particle image velocimetry measurements from cross-correlation peak ratio,” *Measurement Science and Technology*, vol. 24, no. 6, p. 065301, 2013.

Appendix A

FORCE MEASUREMENT CHARTS AT RE = 5.0 X 10^4

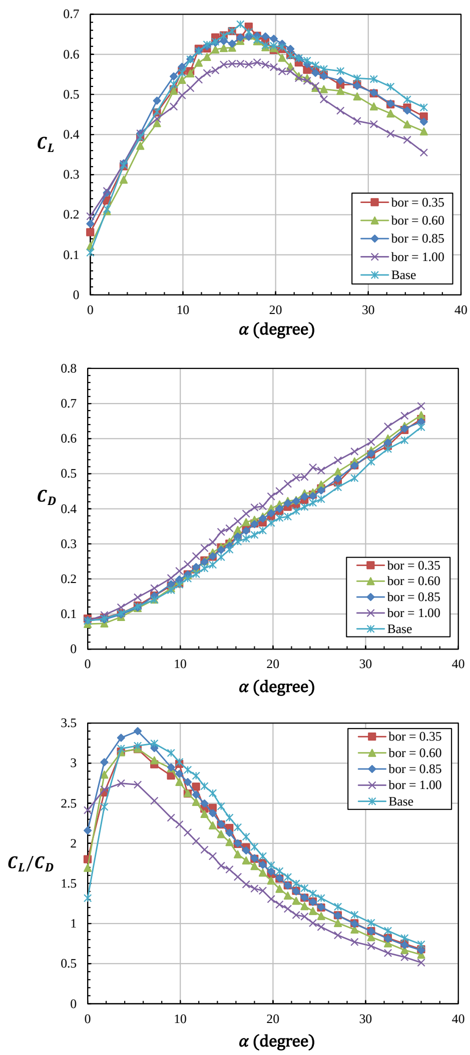

Figure A.1: Non-dimensional lift coefficient C_L, drag coefficient C_D and lift-drag ratio C_L/C_D from top to bottom respectively, for *bor* = 0.35, 0.60, 0.85, 1.00 & Base wings at Re = 5 x 10^4 for $0° \geq \alpha \geq 36°$

Appendix B

FORCE MEASUREMENT RESULTS FOR EACH POINT IN THE CHARTS

Table B.1: Values of each point in the C_L, C_D, C_L/C_D graphs with respect to the corresponding attack angle for *bor* = 0.35, 0.60 and Base wings at Re = 5.0 x 10^4 for $0° \geq \alpha \geq 20.7°$

	Base			*bor*=0.35			*bor*=0.60		
α	C_L	C_D	C_L/C_D	C_L	C_D	C_L/C_D	C_L	C_D	C_L/C_D
0°	0.105	0.08	1.317	0.156	0.087	1.801	0.122	0.072	1.695
1.8°	0.214	0.087	2.455	0.235	0.089	2.634	0.209	0.073	2.857
3.6°	0.324	0.102	3.182	0.321	0.102	3.143	0.287	0.092	3.136
5.4°	0.393	0.122	3.217	0.393	0.124	3.174	0.372	0.117	3.181
7.2°	0.457	0.141	3.245	0.455	0.152	2.985	0.428	0.141	3.036
9°	0.525	0.168	3.128	0.513	0.18	2.844	0.509	0.173	2.935
9.9°	0.554	0.184	3.014	0.559	0.187	2.99	0.536	0.194	2.766
10.8°	0.587	0.201	2.917	0.558	0.213	2.62	0.552	0.21	2.627
11.7°	0.608	0.214	2.843	0.614	0.227	2.706	0.579	0.23	2.516
12.6°	0.624	0.23	2.713	0.614	0.253	2.432	0.593	0.251	2.367
13.5°	0.631	0.24	2.626	0.642	0.263	2.441	0.612	0.275	2.225
14.4°	0.646	0.262	2.463	0.647	0.29	2.234	0.616	0.291	2.115
15.3°	0.658	0.284	2.32	0.658	0.3	2.192	0.617	0.306	2.016
16.2°	0.675	0.307	2.2	0.641	0.322	1.991	0.633	0.34	1.863
17.1°	0.656	0.315	2.083	0.669	0.343	1.95	0.647	0.362	1.787
18°	0.637	0.326	1.956	0.646	0.358	1.806	0.633	0.368	1.717
18.9°	0.623	0.338	1.841	0.633	0.361	1.755	0.618	0.378	1.636
19.8°	0.621	0.36	1.726	0.611	0.378	1.617	0.615	0.401	1.537
20.7°	0.618	0.374	1.653	0.613	0.393	1.56	0.591	0.413	1.433

Table B.2: Values of each point in the C_L, C_D, C_L/C_D graphs with respect to the corresponding attack angle for *bor* = 0.35, 0.60 and Base wings at Re = 5.0 x 10^4 for $21.6° \geq \alpha \geq 36°$

	Base			*bor*=0.35			*bor*=0.60		
α	C_L	C_D	C_L/C_D	C_L	C_D	C_L/C_D	C_L	C_D	C_L/C_D
21.6°	0.597	0.378	1.58	0.598	0.405	1.476	0.57	0.422	1.349
22.5°	0.59	0.394	1.499	0.58	0.412	1.407	0.546	0.425	1.284
23.4°	0.584	0.405	1.442	0.561	0.425	1.322	0.54	0.444	1.218
24.3°	0.573	0.417	1.373	0.561	0.44	1.275	0.516	0.447	1.156
25.2°	0.563	0.428	1.317	0.549	0.458	1.199	0.513	0.469	1.094
27°	0.558	0.461	1.21	0.524	0.475	1.104	0.509	0.506	1.006
28.8°	0.54	0.487	1.109	0.526	0.524	1.004	0.495	0.535	0.925
30.6°	0.538	0.534	1.008	0.502	0.555	0.906	0.47	0.566	0.83
32.4°	0.519	0.571	0.91	0.475	0.579	0.82	0.452	0.6	0.754
34.2°	0.487	0.595	0.819	0.467	0.624	0.748	0.426	0.636	0.669
36°	0.468	0.632	0.739	0.445	0.656	0.678	0.408	0.667	0.612

Table B.3: Values of each point in the C_L, C_D, C_L/C_D graphs with respect to the corresponding attack angle for *bor* = 0.85 & 1.00 wings at Re = 5.0 x 10^4 for $0° \geq \alpha \geq 36°$

	bor=0.85			*bor*=1.00		
α	C_L	C_D	C_L/C_D	C_L	C_D	C_L/C_D
0°	0.177	0.082	2.16	0.196	0.081	2.413
1.8°	0.255	0.085	3.012	0.259	0.097	2.672
3.6°	0.328	0.099	3.317	0.327	0.119	2.749
5.4°	0.403	0.118	3.4	0.403	0.147	2.732
7.2°	0.484	0.152	3.188	0.439	0.174	2.53
9°	0.545	0.185	2.949	0.47	0.202	2.32
9.9°	0.569	0.198	2.867	0.498	0.223	2.236
10.8°	0.588	0.213	2.764	0.516	0.242	2.135
11.7°	0.61	0.234	2.608	0.537	0.265	2.027
12.6°	0.62	0.248	2.497	0.553	0.288	1.92
13.5°	0.629	0.265	2.376	0.56	0.304	1.84
14.4°	0.633	0.283	2.241	0.574	0.334	1.72
15.3°	0.626	0.294	2.131	0.576	0.344	1.675
16.2°	0.642	0.321	2.001	0.577	0.364	1.582
17.1°	0.644	0.337	1.911	0.574	0.386	1.488
18°	0.646	0.356	1.815	0.58	0.404	1.436
18.9°	0.645	0.372	1.732	0.574	0.407	1.41
19.8°	0.639	0.387	1.649	0.568	0.435	1.306
20.7°	0.626	0.4	1.565	0.558	0.45	1.238
21.6°	0.613	0.416	1.475	0.558	0.471	1.184
22.5°	0.59	0.421	1.401	0.541	0.489	1.107
23.4°	0.576	0.435	1.324	0.534	0.491	1.088
24.3°	0.554	0.436	1.269	0.521	0.518	1.006
25.2°	0.546	0.452	1.207	0.488	0.509	0.958
27°	0.534	0.486	1.099	0.459	0.538	0.854
28.8°	0.521	0.523	0.996	0.434	0.563	0.77
30.6°	0.504	0.558	0.904	0.426	0.591	0.721
32.4°	0.477	0.589	0.811	0.402	0.634	0.633
34.2°	0.46	0.628	0.732	0.387	0.665	0.581
36°	0.432	0.648	0.667	0.355	0.693	0.513

Table B.4: Values of each point in the C_L, C_D, C_L/C_D graphs with respect to the corresponding attack angle for *bor* = 0.35, 0.60 and Base wings at Re = 1 x 10^5 for $0° \geq \alpha \geq 36°$

	Base			*bor*=0.35			*bor*=0.60		
α	C_L	C_D	C_L/C_D	C_L	C_D	C_L/C_D	C_L	C_D	C_L/C_D
0°	0.133	0.065	2.032	0.122	0.070	1.736	0.150	0.074	2.026
1.8°	0.267	0.077	3.451	0.223	0.073	3.045	0.263	0.074	3.541
3.6°	0.368	0.096	3.844	0.327	0.091	3.608	0.347	0.094	3.706
5.4°	0.452	0.122	3.709	0.410	0.116	3.539	0.439	0.124	3.547
7.2°	0.524	0.148	3.550	0.464	0.141	3.290	0.490	0.146	3.350
9°	0.592	0.180	3.287	0.520	0.171	3.043	0.569	0.182	3.116
9.9°	0.625	0.196	3.191	0.558	0.191	2.929	0.599	0.200	2.993
10.8°	0.653	0.214	3.055	0.587	0.209	2.808	0.620	0.215	2.881
11.7°	0.685	0.233	2.938	0.617	0.229	2.691	0.648	0.238	2.724
12.6°	0.711	0.253	2.811	0.644	0.248	2.598	0.675	0.261	2.586
13.5°	0.725	0.272	2.661	0.667	0.271	2.461	0.694	0.282	2.464
14.4°	0.736	0.292	2.518	0.680	0.292	2.334	0.703	0.298	2.360
15.3°	0.736	0.309	2.377	0.676	0.305	2.219	0.708	0.319	2.222
16.2°	0.741	0.328	2.263	0.669	0.319	2.095	0.705	0.333	2.116
17.1°	0.748	0.348	2.152	0.675	0.341	1.976	0.713	0.354	2.012
18°	0.729	0.358	2.039	0.663	0.352	1.885	0.716	0.373	1.919
18.9°	0.713	0.370	1.924	0.662	0.372	1.778	0.703	0.384	1.831
19.8°	0.688	0.374	1.841	0.654	0.385	1.700	0.702	0.403	1.740
20.7°	0.674	0.387	1.741	0.631	0.394	1.601	0.686	0.418	1.643
21.6°	0.669	0.404	1.655	0.618	0.405	1.527	0.671	0.428	1.570
22.5°	0.658	0.415	1.586	0.599	0.413	1.450	0.642	0.432	1.487
23.4°	0.653	0.434	1.505	0.591	0.427	1.385	0.627	0.446	1.406
24.3°	0.644	0.448	1.435	0.577	0.441	1.310	0.611	0.454	1.344
25.2°	0.634	0.459	1.380	0.571	0.456	1.250	0.594	0.460	1.291
27°	0.620	0.487	1.273	0.549	0.476	1.155	0.585	0.496	1.179
28.8°	0.608	0.520	1.168	0.541	0.512	1.056	0.566	0.520	1.087
30.6°	0.592	0.555	1.067	0.524	0.544	0.963	0.550	0.559	0.983
32.4°	0.567	0.585	0.969	0.501	0.575	0.870	0.529	0.591	0.895
34.2°	0.552	0.624	0.885	0.479	0.605	0.791	0.508	0.624	0.814
36°	0.536	0.659	0.813	0.466	0.640	0.728	0.495	0.661	0.749

Table B.5: Values of each point in the C_L, C_D, C_L/C_D graphs with respect to the corresponding attack angle for *bor* = 0.85 & 1.00 wings at Re = 1 x 10^5 for $0° \geq \alpha \geq 36°$

	bor=0.85			*bor*=1.00		
α	C_L	C_D	C_L/C_D	C_L	C_D	C_L/C_D
0°	0.235	0.072	3.241	0.206	0.083	2.495
1.8°	0.315	0.083	3.812	0.302	0.098	3.091
3.6°	0.412	0.107	3.862	0.372	0.121	3.081
5.4°	0.503	0.138	3.656	0.435	0.151	2.887
7.2°	0.557	0.165	3.373	0.482	0.179	2.688
9°	0.622	0.198	3.143	0.537	0.215	2.499
9.9°	0.644	0.210	3.068	0.557	0.230	2.423
10.8°	0.672	0.232	2.891	0.586	0.254	2.308
11.7°	0.697	0.250	2.785	0.601	0.270	2.223
12.6°	0.713	0.270	2.645	0.621	0.291	2.138
13.5°	0.737	0.290	2.541	0.632	0.307	2.057
14.4°	0.752	0.310	2.422	0.645	0.330	1.955
15.3°	0.747	0.325	2.302	0.652	0.349	1.867
16.2°	0.756	0.351	2.154	0.653	0.366	1.784
17.1°	0.756	0.368	2.057	0.661	0.387	1.708
18°	0.765	0.391	1.957	0.670	0.413	1.622
18.9°	0.758	0.401	1.887	0.666	0.426	1.562
19.8°	0.760	0.423	1.794	0.639	0.431	1.481
20.7°	0.750	0.438	1.712	0.635	0.449	1.416
21.6°	0.733	0.447	1.637	0.627	0.466	1.347
22.5°	0.716	0.457	1.567	0.615	0.478	1.288
23.4°	0.697	0.469	1.486	0.594	0.483	1.229
24.3°	0.675	0.476	1.420	0.583	0.496	1.174
25.2°	0.672	0.494	1.359	0.564	0.505	1.117
27°	0.636	0.512	1.243	0.536	0.526	1.018
28.8°	0.622	0.541	1.149	0.517	0.550	0.940
30.6°	0.602	0.579	1.040	0.500	0.582	0.860
32.4°	0.575	0.607	0.949	0.488	0.614	0.794
34.2°	0.557	0.641	0.869	0.468	0.643	0.728
36°	0.540	0.674	0.802	0.449	0.671	0.669

Appendix C

MATLAB CODE TO CALCULATE VELOCITY MAGNITUDE RMS

```
clear all
clc
NAME =  bor1Re5018deg2,7mm1728x1952
firstFrameNumber = 10;
lastFrameNumber  = 209;
fileNumber = firstFrameNumber:lastFrameNumber;
Expname =  Solidity000 ;
extension =  .T000.D000.P000.H000.L.vec ;

L=1;
for i=fileNumber(1):fileNumber(length(fileNumber))
    if i   10
        fileNames L  = strcat(Expname, 0 ,num2str(fileNumber(L)),
            extension);
    end
    if i  = 10    i   100
        fileNames L  = strcat(Expname, 0 ,num2str(fileNumber(L)),
            extension);
    end
    if i  = 100
        fileNames L  = strcat(Expname,num2str(fileNumber(L)),
            extension);
    end
    L=L+1;

end
pwd
for i=1:(lastFrameNumber firstFrameNumber+1)
```

```
    [vecfile, details]=fopen(fileNames i , r );

    firstline = fgetl(vecfile);   reads the first line
    firstline = split(firstline);
    I = str2num(erase(firstline 4 3 , I= ));   get the mesh number
    J = str2num(erase(firstline 4 4 , J= ));   get the mesh number

    holder = fgetl(vecfile);   reads the second line
    k=1;
    while(holder = 1 )
        holder = strrep(holder,  ,  ,    );
        holder = str2num(holder);

        Data(k,:,i) = holder;
        Data2(i,k,:) = holder;
        k = k+1;
        holder = fgetl(vecfile);
    end

    fclose(vecfile);
end



X(:,:) = Data(:,1,1);
Y(:,:) = Data(:,2,1);
U(:,:) = Data(:,3,:);
V(:,:) = Data(:,4,:);

for i=1 : length(U)
    for j=1 : (lastFrameNumber firstFrameNumber+1)
        velmag(i,j) = sqrt(U(i,j) 2 + V(i,j) 2 );
    end
end

for i=1 : length(U)
    meanvelmag(i) = mean(velmag(i,:));   calculates the mean of
```

```
        set of data for each IA
end


for i=1 : length(U)
    meanU(i) = mean(U(i,:));   calculates the mean of set of data
        for each IA
    meanV(i) = mean(V(i,:));   calculates the mean of set of data
        for each IA
    meanvelmag(i) = mean(velmag(i,:));   calculates the mean of
        set of data for each IA
end
for i=1 : length(U)
    diffU(i,:) = U(i,:) meanU(i);   subtracts the mean for the
        value of each IA
    diffV(i,:) = V(i,:) meanV(i);   subtracts the mean for the
        value of each IA
    diffvelmag(i,:) = velmag(i,:) meanvelmag(i);   calculates
        the mean of set of data for each IA
end
for i=1 : length(U)
    SqrdiffU(i,:) = diffU(i,:).2;
    SqrdiffV(i,:) = diffV(i,:).2;
    Sqrdiffvelmag(i,:) = diffvelmag(i,:).2;
end
for i=1 : length(U)
    rmsvalues(i,1) = sqrt(sum(SqrdiffU(i,:)) / length(U(i,:)));
    rmsvalues(i,2) = sqrt(sum(SqrdiffV(i,:)) / length(V(i,:)));
    rmsvalues(i,3) = sqrt(sum(Sqrdiffvelmag(i,:)) / length(
        velmag(i,:)));
end

TecplotWriter(X,Y,rmsvalues,NAME,I,J);
```

Appendix D

MATLAB CODE TO CONVERT RMS CALCULATIONS INTO THE TECPLOT FILE

```
function [] = TecplotWriter(X,Y,A, name,II,JJ)
U = A(:,1);
V = A(:,2);
VelMag = A(:,3);
file = fopen(strcat(name, RMS.dat ), wt );

fprintf(file, s s s , TITLE = " , name, " );
fprintf(file, s , VARIABLES = "X mm", "Y mm", "Urms", "Vrms" ,"
   VelocityMagnituderms");
fprintf(file, s s i s i s n , ZONE T="ZONE 001" , ,I= ,II
   , , J= , JJ, , F=POINT );

for i = 1:II JJ
 fprintf(file, .10f t .10f t .10f t .10f t .10f n ,X(i),Y(i),U(i)
     ,V(i),VelMag(i));
end
fclose(file);
end
```